Astronomy & Astrophysics manuscript no. trio˙grbSNe
March 16, 2014

A Trio of GRB-SNe

Z. Cano[1], A. de Ugarte Postigo[2,3], A. Pozanenko[4], N. Butler[5], C. C. Thöne[2], C. Guidorzi[6], T. Krühler[3,7], J. Gorosabel[8,9,10], P. Jakobsson[1], G. Leloudas[18,3], C. Mundell[11], A. Melandri[12], K. Wiersema[13], P. D'Avanzo[12], S. Schulze[14,15], A. Gomboc[16,17], D. Malesani[3], A. Johansson[1], W. Zheng[19], D. A. Kann[20,21], F. Knust[20], K. Varela[20], C. W. Akerlof[22], O. Burkhonov[31], E. Cooke[30], G. Dhungana[23], C. Farina[29], F. V. Ferrante[23], H. A. Flewelling[24], J. Fynbo[3], J. Greiner[20], T. Güver[25], O. Hartoog[26], N. Hatch[39,40], J. Hjorth[3], R. Kehoe[23], S. Klose[21], E. Klunko[32], Y. Krugly[33], A. Levan[27], V. Linkov[34], A. Matkin[35], N. Minikulov[36], I. Molotov[37], V. Rumyantsev[38], R. Sánchez-Ramírez[2], I. Steele[11], N. Tanvir[13], A. Volnova[4], D. Xu[3], and F. Yuan[28]

(Affiliations can be found after the references)

Received xx xxx 2014 / Accepted xx xxx 2014

ABSTRACT

We present optical and near-infrared (NIR) photometry for three gamma-ray burst supernovae (GRB-SNe): GRB 120729A, GRB 130215A / SN 2013ez and GRB 130831A / SN 2013fu. Additionally, we present spectroscopic observations of SN 2013ez, where undulations are seen in the optical spectrum that are reminiscent of other GRB-SNe. A blueshifted Fe II $\lambda5169$ absorption feature at $v \approx 4000$ km s^{-1} at $t - t_0 = 16.1$ d in the rest-frame, indicating that it is of type Ic, making it the first GRB-SNe to not be classified as a type Ic-BL. We have determined the brightness and shape of each accompanying SN relative to a template supernova (SN 1998bw), and in doing so we make estimates of the amount of nickel nucleosynthesized during each explosion. We find that our derived nickel masses are typical of other GRB-SNe, and greater than those of SNe Ibc that are not associated with GRBs. For GRB 130831A / SN 2013fu, we use our well-sampled R-band light curve (LC) to estimate the amount of ejecta mass and the kinetic energy of the SN, finding that these too are typical of other GRB-SNe. For GRB 130215A, we take advantage of contemporaneous optical/NIR observations obtained by RATIR and GROND to construct an optical/NIR bolometric LC of the afterglow. We fit the bolometric LC with the millisecond magnetar model of Zhang & Mészáros (2001), which considers dipole radiation as a source of energy injection to the forward shock powering the optical/NIR afterglow. Using this model we derive an initial spin period of $P = 12$ ms and a magnetic field of $B = 1.1 \times 10^{15}$ G, which are similar to those found for magnetar central engines of other long-duration GRBs.

Key words. words. that are about keys.

1. Introduction

Observational evidence supporting the connection between long-duration gamma-ray bursts (GRBs) and stripped-envelope, core-collapse supernovae (SNe) is now quite extensive (see Woosley & Bloom, 2006, and Hjorth & Bloom 2012 for extensive reviews of gamma-ray burst supernovae; GRB-SNe). 2013 was a prosperous year for GRB-SN science, with no less than four spectroscopic GRB-SN associations: GRB 130215A / SN 2013ez (de. Ugarte Postigo et al. 2013b); GRB 130427A / SN 2013ez (de Ugarte Postigo et al. 2013d; Xu et al. 2013a; Levan et al. 2013; Melandri et al. 2014); GRB 130702A / SN 2013dx (Schulze et al. 2013) and GRB 130831A / SN2013fu (Klose et al. 2013; Nicuesa Guelbenzu et al. 2013). These events join other spectroscopic GRB-SN associations (Galama et al. 1998; Hjorth et al. 2003; Stanek et al. 2003; Malesani et al. 2004; Pian et al. 2006; Chornock et al. 2010; Bufano et al. 2012; Berger et al. 2011; Sparre et al. 2010; Klose et al. 2012; Schulze et al. 2014). Numerous photometric inferences of GRB-SNe via "SN bumps" in optical and near-infrared (NIR) light-curves (LCs) further strengthen the GRB-SN connection (see e.g. Cano 2013 for a review).

The favoured physical description for producing a GRB is the "collapsar" scenario (Woosley 1993; MacFadyen & Woosley 1999; MacFadyen et al. 2001), where a compact object forms during the collapse of a massive star and ejects shells of material at relativistic velocities. Multiple shells interact producing the initial γ-ray pulse, and as they propagate away from the explosion they encounter circumstellar material (CSM) ejected by the progenitor star prior to explosion (as well as interstellar material), producing a long-lived afterglow (AG). In the simplest scenario, a forward shocks (FS) is thought to be created when the shells interact with the CSM, which accelerate electrons that cool by emitting synchrotron radiation. A couple of weeks (rest-frame) after the initial γ-ray pulse energetic SNe are then observed at optical and NIR wavelengths.

A basic assertion of the collapsar model is that the duration of the GRB pulse is the difference between the time that the central engine operates minus the time it takes for the jet to breakout of the star: $T_{90} = t_{\rm engine} - t_{\rm breakout}$. A direct consequence of this premise is that there should be a plateau in the distribution of T_{90} for GRBs produced by collapsars when $T_{90} < t_{\rm breakout}$, which was observed by Bromberg et al. (2012). Moreover, the value of T_{90} found at the upper-limit of the plateau seen in all three satellites was approximately the same ($T_{90} \sim 20 - 30$ s), which is the "typical" breakout time of the jet. This short breakout time suggests that the progenitor star at the time of explosion is very compact ($\sim 5\ R_{\odot}$; Piran et al. 2012). Bromberg et al. (2013) then used these distributions to calculate the probability that a given GRB arises from a collapsar or not based on its T_{90} and hardness ratio.

The theoretical and observational evidence for the GRB-SNe connection is strong, however some questions remain unan-

Send offprint requests to: e-mail: zewcano@gmail.com

swered. One of the biggest uncertainties is the nature of the compact object that powers the GRB, and whether it is a stellar black hole rapidly accreting mass from a torus or a neutron star with a very large magnetic field (10^{15-16} Gauss) and rotating near breakup ($P \approx 1$ ms; i.e. a millisecond magnetar), or both. Numerous flares and plateaus have been seen in AG LCs at X-ray and optical wavelengths (e.g. Margutti et al. 2010; Grupe et al. 2007, 2010), which require energy injection from a central engine. The origin of the energy injection is still uncertain however, and may arise from different sources in different events.

Secondly, the nature of the progenitor system has yet to be determined. Due to the vast cosmological distances that GRBs occur it is not possible to detect the progenitor directly, as have been done for the progenitors of other types of core-collapse SNe (e.g. Smartt et al. 2009; Maund et al. 2014). Instead, the possible configuration of the progenitor system has to be indirectly inferred, where it is a formidable challenge to resolve the ambiguity between single and binary stars. Arguments based on statistically significant sample sizes of the bolometric properties of GRB-SNe in relation to the other SN Ibc subtypes (Ib, Ic and Ic-BL; Cano 2013) indicate that the progenitors of most SNe Ibc likely arise from binary systems, where the mass of individual stars in the system is less than that is attributed to single Wolf-Rayet stars observed in nature (Crowther et al. 2007). In these systems the outer layers of the star are tidally stripped, as well as ejected via line-driven winds. Conversely, the progenitors of SNe Ic-BL and GRB-SNe may arise from more massive single-star progenitors, where the former are more metal rich than the latter (though see as well Levesque et al. 2012, Krühler et al. 2012, Savaglio et al. 2012 and Elliott et al. 2013 who have shown, respectively, that GRBs 020819, 080605, 090323 and 110918A occurred in galaxies of solar and super-solar metallicities), and therefore lose more mass before exploding than GRB-SNe. This provides a natural explanation for why a high-energy transient is observed in the latter because the central engine that is formed has retained more angular momentum at the time of explosion. However, GRBs may also arise via binary systems, where the system may undergo a common-envelope phase. If the system remains intact after one of the stars explodes, the inspiral of the compact object into the core of the unexploded secondary can impart angular momentum to the core, which may be retained at the time of explosion to then power a GRB.

In this paper we attempt to address at least one of these outstanding questions, namely the nature of the compact object central engine of GRB 130215A. Using the model of Zhang & Mészáros (2001) we show that energy injection from a millisecond magnetar provides a plausible fit to an optical/NIR bolometric LC of the AG. Using simple assumptions of the magnetar's mass and radius we derive physically plausible estimates of it's magnetic field strength and initial spin period. The other focus of this work is an investigation of the observational and physical properties of three GRB-SNe. In sections 2, 3 and 4 we present photometric and spectroscopic observations of GRB 120729A, GRB 130215A / SN 2013ez and GRB 130831A, respectively. A SN signature is seen in each event, which arises via SN-bumps for GRBs 120729A and 130831A, and a bump+spectrum for GRB 130215A. In section 5 we discuss the observational and physical properties of these three GRB-SNe in relation to other SNe Ibc.

Throughout this paper we use a Planck cosmology (Planck Collaboration et al. 2013) of $H_0 = 67.3$ km s^{-1} Mpc^{-1}, $\Omega_M = 0.315$, $\Omega_\Lambda = 0.685$. Foreground extinction has be calculated using the dust extinction maps of Schlegel et al. (1998), while values of the rest-frame extinction that have been derived from our data are presented in Table 1. All bolometric properties (nickel mass, ejecta mass and kinetic energy, $M_{\rm Ni}$, $M_{\rm ej}$ and $E_{\rm K}$ respectively) are calculated for the rest-frame filter range $UBVRIJH$ using the method in Cano (2013; C13 hereon). Unless stated otherwise, errors are statistical only. Observer-frame times are used unless specified otherwise in the text. The respective decay and energy spectral indices α and β are defined by $f_\nu \propto (t - t_0)^{-\alpha} \nu^{-\beta}$, where t_0 is the time of burst.

2. GRB 120729A

GRB 120729A was detected at 10:56:14 UT on 29-July-2012 by the *Swift* Burst Alert Telescope (BAT), and has a $T_{90} = 71.5 \pm 17.5$ s in the 15–350 keV energy range (Ukwatta et al. 2012; Palmer et al. 2012). It was also detected by the *Fermi* Gamma-Ray Burst Monitor (GBM) with a $T_{90} \approx 25$ s in the 50–300 keV energy range (Rau 2012). Rapid follow-up by several ground-based telescopes identified an optical transient coincident with the XRT position (Virgili et al. 2012; Oates & Ukwatta, 2012; Im & Hong, 2012, Wren et al. 2012; Gorosabel et al. 2012; D'Avanzo et al. 2012), and a redshift of $z = 0.80$ was measured with Gemini-North (Tanvir & Ball, 2012). The AG was not detected at radio (Laskar et al. 2012) or sub-mm wavelengths (Smith et al. 2012) down to 3σ upper limits of 39 μJy and 58 μJy, at 5.8 and 21.8 GHz, respectively. An estimate of of the isotropic energy release in γ-rays (1–10^4 keV, rest-frame) is $E_{\rm iso,\gamma} = 2.3^{+0.3}_{-1.5} \times 10^{52}$ erg[1]. The probability that GRB 120729A arises from a collapsar (Bromberg et al. 2013) based on T_{90} alone is $99.996 \pm 0.001\%$ (BAT) and $98.225 \pm 1.004\%$ (GBM). We have used a foreground extinction value of $E(B-V)_{\rm fore} = 0.164$ mag (Schlegel et al. 1998) for GRB 120729A.

2.1. Data Reduction & Photometry

We obtained observations with the 2-m Faulkes Telescope North (FTN) robotic telescope starting less than ten minutes after the γ-ray detection. Subsequent follow-up observations were obtained with the 2-m Liverpool Telescope (LT), the 0.82-m Instituto de Astrofísica de Canarias (IAC) IAC80 telescope, the 3.6-m Telescopio Nazionale Galileo (TNG), and the 10.4-m Gran Telescopio Canarias (GTC) telescope. Six epochs of GTC images in *griz* were obtained during the first month, and a final epoch in all filters at $t - t_0 \approx 190$ d that was used as templates for image subtraction. Image reduction of data obtained on all telescopes were performed using standard techniques in IRAF[2].

Calibration of the GTC data has been performed using standard star photometry. Observations (in *griz*) of Landolt standard field PG1323-086 (Landolt 1992) were obtained the same night as the final GTC epoch, all of which were taken under photometric conditions. The BVR_cI_c magnitudes of PG1323-086 were transformed into *griz* using transformation equations from Jordi et al. (2006), and the subsequent calibration was done using a zeropoint between the instrumental and catalog magnitudes. The calibration in each filter was then used to create a set of secondary standards in the GRB field, which the GTC images are calibrated against.

The BVR_cI_c FTN, LT and TNG images are shallower than the GTC ones, where common stars are either saturated in the

[1] http://butler.lab.asu.edu/swift/bat_spec_table.html

[2] IRAF is distributed by the National Optical Astronomy Observatory, which is operated by the Association of Universities for Research in Astronomy, Inc., under cooperative agreement with the National Science Foundation.

Table 1. GRB-SNe: Vital Statistics

GRB	SN	z	$A_{V,\mathrm{fore}}$ (mag)	$A_{V,\mathrm{rest}}$ (mag)	$d_L^{\dagger}$ (Mpc)
120729A	-	0.80	0.55	0.15	4910.7
130215A	2013ez	0.597	0.53	0.00	3502.2
130831A	2013fu	0.479	0.15	0.00	2664.2

† Luminosity distance calculated using $H_0 = 67.3$ km s^{-1} Mpc^{-1}, $\Omega_M = 0.315$, $\Omega_\Lambda = 0.685$.

GTC images or not visible in the FTN/LT ones. Instead these images have been independently calibrated via standard star photometry using Landolt standards taken with the TNG the same night as the GRB observations. A zeropoint was computed between the Landolt standards and the instrumental BVR_cI_c magnitudes, which was then used to create a small set of secondary standards in the GRB field that were visible in all FTN/LT/TNG images but not saturated. The BVR_cI_c magnitudes were then transformed into *gri* magnitudes using transformation equations from Jordi et al. (2006), which requires colours between filters (e.g. $R_c - I_c$) in order to properly calculate the corresponding SDSS magnitudes. Early observations in R_c and I_c were taken within 5–10 minutes of each other, however, as these observations were taken very soon after the initial GRB trigger (after only a few tens of minutes), it may not be appropriate to assume no colour/spectral evolution during the timing of a given R-band and I-band observation. Instead we have estimated magnitudes in R_c and I_c at the times of each filter (e.g. estimating R_c for a given I_c observation, and visa versa) by two methods: (1) a log-linear interpolation of the LC, and (2) fitting a broken PL to the LCs in order to extrapolate to earlier and later times. When possible we have taken the average magnitude found with both of these methods, and included their standard deviation when calculating the SDSS magnitude in *gri*.

We used our deep GTC images to obtain image-subtracted magnitudes of the optical transient (OT) associated with GRB 120729A, using the final epoch in each filter as a template. This method proved to be valuable to isolate the OT flux as the field is quite crowded, and because the OT is very faint. Already at $t - t_0 = 0.75$ d the *griz* magnitudes of the OT are m_{AB} =24–25. Image subtraction was performed using an adaptation of the original ISIS program (Alard & Lupton 1998; Alard 2000) that was developed for Hubble Space Telescope SN surveys by Strolger et al. (2004). A key advantage of this code is the option for the user to specify a set of "stamps" for the program to use when it calculates the point-spread function in each image. The image-subtraction technique was then optimised by varying the kernel mesh size and measuring the standard deviation (σ) of the background counts in a nearby region in the image (where images with lower σ values indicate they are a "better" subtracted image). As a self-consistency check, we compared the OT magnitudes against those found by performing photometry on the un-subtracted images, converting the magnitudes into fluxes, and then mathematically subtracting the host flux away. Good agreement was obtained with both methods, showing that the image-subtraction technique was well optimised.

The *griz* magnitudes of the host galaxy were measured, and these magnitudes were converted into monochromatic fluxes using the flux zeropoints from Fukugita et al. (1995) and subtracted from the earlier observations obtained with the LT, FTN and IAC80. The apparent magnitudes (not corrected for foreground or host extinction) of the GRB+SN+host are presented in Table 6.

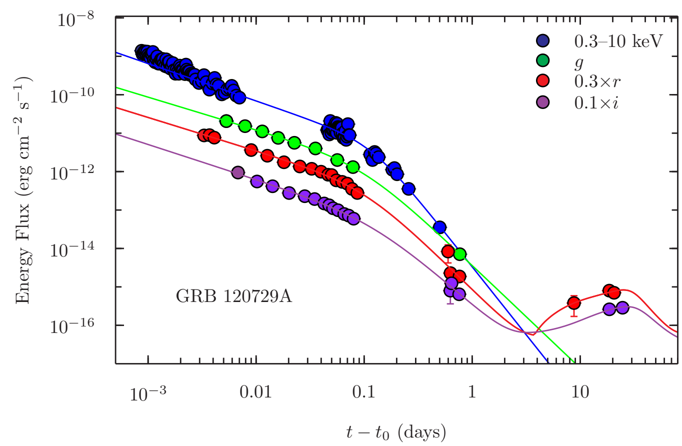

Fig. 1. GRB 120729A: Optical and X-ray (0.3–10 keV) light curves. BR_cI_c magnitudes have been transformed into *gri* using transformation equations from Jordi et al. (2006), see the main text for details. The optical data are "host-subtracted" and have been corrected for foreground and rest-frame extinction. All LCs have been fit with a broken power-law in order to determine the decay rate before ($\alpha_{\nu,1}$) and after ($\alpha_{\nu,2}$) and the break ($T_{\nu,\mathrm{B}}$), as well as the timing of the break. It is seen that α_1 is approximately the same in the optical and X-ray, as well as the time of the break ($T_\mathrm{B} \approx 0.1$ d). After the break the X-ray decays at a faster rate than the optical filters. In r and i we have simultaneously fit a SN-component (i.e. a stretch and luminosity factor relative to a redshifted, k-corrected template LC). The paucity of optical points limits our analysis, however when fixing the stretch factor to $s = 1.0$, we find luminosity factors of $k_r = 1.29 \pm 0.19$ and $k_i = 0.76 \pm 0.11$.

2.2. The Afterglow

We have combined our optical detections with the *Swift* XRT (0.3–10 keV) observations (Fig. 1), where our foreground and rest-frame-corrected, host-subtracted magnitudes have been converted into monochromatic fluxes (mJy), and then into energy fluxes (erg cm^{-2} s^{-1}) using the zeropoints and filter effective wavelengths from Fukugita et al. (1995).

We have fit all LCs with a broken power-law (PL) (we have also included a "SN-component" that is simultaneously determined when fitting the r and i LCs, see section 2.5) in order to determine the decay rate before ($\alpha_{\nu,1}$) and after ($\alpha_{\nu,2}$) and the break ($T_{\nu,\mathrm{B}}$), and the timing of the break. Our best-fitting parameters (fit between 0.005–30 d) are: (1) X-ray: $\alpha_{X,1} = -0.97 \pm 0.06$, $\alpha_{X,2} = -3.54 \pm 0.27$, $T_{X,\mathrm{B}} = 0.12 \pm 0.02$ d; (2) optical: $\alpha_{g,1} = -0.85 \pm 0.04$, $\alpha_{g,2} = -2.67 \pm 0.13$, $T_{g,\mathrm{B}} = 0.10 \pm 0.02$ d; $\alpha_{r,1} = -0.87 \pm 0.03$, $\alpha_{r,2} = -2.77 \pm 0.10$, $T_{r,\mathrm{B}} = 0.10 \pm 0.02$ d; $\alpha_{i,1} = -0.91 \pm 0.08$, $\alpha_{i,2} = -2.49 \pm 0.20$, $T_{i,\mathrm{B}} = 0.12 \pm 0.04$ d. The time the LC breaks is approximately the same time at all frequencies ($T_\mathrm{B} \approx 0.1$ d). The value of α_1 is roughly the same at all wavelengths before the break, and while α_2 is steeper in the X-ray than the optical, it is quite similar in all optical bands.

If the achromatic break at $t-t_0 \approx 0.11$ d is interpreted as a jet break, it is possible to estimate the angular width of the jet using equation 4 in Piran (2004). Assuming a density of $n = 1$ cm^{-3}, and an isotropic kinetic energy in the ejecta $\equiv \eta E_{\mathrm{iso},\gamma}$, where η is the radiative efficiency and we have assumed a value of $\eta = 0.2$, we estimate an opening angle of $\theta \approx 4.4^{\circ}$. In turn this implies a beaming-corrected γ-ray energy release of $E_{\theta,\gamma} = (\frac{\theta^2}{2})E_{\mathrm{iso},\gamma} \approx 6.8\times10^{49}$ erg. If the density is higher, $n = 10$, the opening angle is larger ($\theta \approx 5.7^{\circ}$), and so is the beam-corrected kinetic energy ($E_{\theta,\gamma} \approx 1.2\times10^{50}$ erg).

2.3. The Spectral Energy Distribution

We have combined our host-subtracted GTC magnitudes at $t-t_0 = 0.75$ d, which were corrected for foreground extinction and converted into monochromatic fluxes, with contemporaneous X-ray observations to construct an X-ray to optical spectral energy distribution (SED), with the intention of getting an estimate of the amount of rest-frame extinction (Fig. 2). We have followed the general procedure as outlined in Guidorzi et al. (2009) when constructing the energy spectrum. As there are fewer X-ray photons at late times (the final observation is at $t-t_0 = 0.5$ d), the X-ray spectrum has been assembled using photons detected just before the break, and the LC was extrapolated to the time of the optical data using a broken PL and a normalization coefficient.

Both a single ($\beta_X = \beta_O$) and broken PL ($\beta_X - \beta_O = 0.5$, which is fixed) were fit to the SED, where it was found that a cooling break was not needed to fit the data, with a spectral index of $\beta = 1.0 \pm 0.1$ proving to be a good fit. When a cooling break was imposed upon the data, it was always found to occur below the optical data. The paucity of data does not allow us to discriminate between the different extinction curves of the Small Magellanic Cloud (SMC), Large Magellanic Cloud (LMC) and Milky Way (MW) from Pei (1992), so we have adopted an SMC template (which has proved to be a suitable fit to the AG SEDs, e.g. Kann et al. 2006). Our best-fitting parameters ($\chi^2/dof = 29.6/28$) are $A_V = 0.15$ mag (< 0.55 at 90% CL), and an intrinsic column absorption of $N_{\mathrm{H}} = 1.0\times10^{21}$ cm^{-2} ($< 0.27\times10^{21}$ at 90% CL). To convert the rest-frame extinction into equivalent observer-frame extinctions in our SDSS filters, we have used the SMC extinction template at $z = 0.8$ and the effective wavelengths in Fukugita et al. (1995), finding: $A_{g,obs} = 0.34$ mag, $A_{r,obs} = 0.26$ mag and $A_{i,obs} = 0.20$ mag. We have used these value of the rest-frame extinction throughout our analysis of GRB 120729A.

2.4. The Host Galaxy

We have used our *griz* observations of the host galaxy, taken at $t-t_0 \approx 189$ d and corrected for foreground extinction, to constrain some of its key physical properties (Fig. 3). Our procedure involves fitting the photometry with stellar population synthesis models from Bruzual & Charlot (2003) with LePHARE (Arnouts et al. 1999). We use a Calzetti dust attenuation law (Calzetti et al. 2000), a Chabrier initial mass function (Chabrier, 2003) and a grid of different star-burst ages with varying *e*-folding timescales to derive theoretical galaxy spectra which then were compared to our photometry. A more elaborate description of our SED fitting procedure and its caveats is given in Krühler et al. (2011).

The best fitting template is for that of a low-mass, blue, young star-forming galaxy. The best-fitting parameters are: $M_B = -19.3 \pm 0.1$, $\log_{10}$(mass)=8.3 ± 0.2 $M_\odot$, SFR= 6^{+25}_{-4} $M_\odot$ yr^{-1} and the age of the starburst ≤ 100 Myr. The SFR has a large uncertainty due to the unknown dust attenuation.

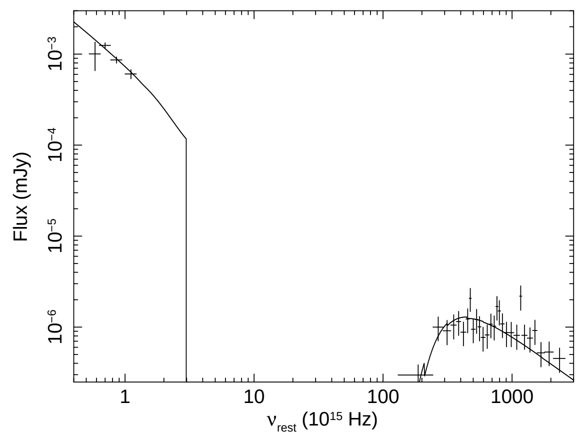

Fig. 2. GRB 120729A: Rest-frame X-ray to optical SED of the AG at $t-t_0 = 0.42$ d. It is found that a single PL provides a good fit to the data, with $\beta = 1.0 \pm 0.1$. Our best-fitting parameters ($\chi^2/dof = 29.6/28$) are $A_V = 0.15$ mag (< 0.55 at 90% CL), and an intrinsic column absorption of $N_{\mathrm{H}} = 1.0\times10^{21}$ cm^{-2} ($< 0.27\times10^{21}$ at 90% CL).

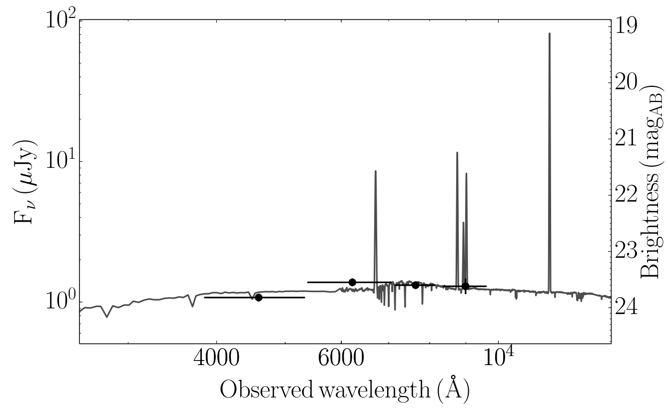

Fig. 3. GRB 120729A: Best-fitting SED of the host galaxy *griz* magnitudes. The best fitting template is for a low-mass ($\log_{10}$(mass)=8.3 ± 0.2 $M_\odot$), blue, star-forming galaxy (SFR= 6^{+25}_{-4} $M_\odot$ yr^{-1} and the age of the starburst ≤ 100 Myr).

2.5. The Supernova

The dearth of late-time observations limits our analysis of the accompanying SN to GRB 120729A, where only a few detections have been made near peak in *r* and *i*. Indeed the shape of the SN LC is not well constrained, especially given the lack of detections after the peak. Nevertheless, despite this limitation we have estimated the brightness of the SN in both filters during our fit. In addition to fitting broken power-laws to LCs, we have included an additional SN-component. Using the C-program written by C. Guidorzi, which is presented in C13[3], we have created synthetic, k-corrected LCs of a template LC (SN 1998bw) as it would appear if it occurred at $z = 0.80$. Then using Pyxplot[4] we fit the synthetic LC with a linear spline. This spline is then incor-

[3] see as well Cano (2014, in prep.)

[4] http://pyxplot.org.uk

porated into another function (equation 5 in C13) that transforms it by a stretch (s) and luminosity (k) factor. In events where there are many observations of the SN bump (e.g. GRB 130427A / SN 2013cq, Xu et al. 2013a) it is possible to constrain both s and k, however here we have fixed $s = 1.0$ and allowed only k to be a free parameter during the fit. Our best-fitting parameters are: $k_r = 1.29 \pm 0.19$ and $k_i = 0.76 \pm 0.11$. Taking these at face value implies (observer-frame) peak absolute magnitudes of $M_{r,\rm peak} = -18.96 \pm 0.15$ and $M_{i,\rm peak} = -19.29 \pm 0.15$, though these are somewhat tentative at best due to the uncertain stretch-factor of the SN, where a larger stretch factor implies a brighter luminosity. With the same reasoning we have not attempted to estimate the time of peak light in each filter.

Using the method presented in C13, we have estimated the bolometric properties of the accompanying SN. Given that we have not been able to constrain the shape (i.e. width) of the SN in either filter, there is little merit in estimating its ejecta mass and in turn its kinetic energy. However we can make an estimate of the amount of nickel that was nucleosynthesized during the explosion using "Arnett's Rule" (Arnett 1982) – i.e. the luminosity at maximum is proportional to the instantaneous energy deposition from the radioactive decay of nickel and cobalt. Making the assumption that the average luminosity factor of the accompanying SN in the optical filters is a suitable proxy for the relative difference in luminosity between this SN and the template, (which was shown in C13 to have an uncertainty of order 10%), and using an average luminosity factor of $\bar{k} = 1.02 \pm 0.26$, and fixing $s = 1.0$, we estimate that in the filter range $UBVRIJH$ the accompanying SN has a nickel mass of $M_{\rm Ni} = 0.42 \pm 0.11\ M_{\odot}$. The quoted error is statistical only, and arises from the uncertainty in the luminosity factor. This nickel mass is close to that estimated for the archetype GRB-SN 1998bw, where it is estimated 0.4–0.7 $M_{\odot}$ was nucleosynthesized (Iwamoto et al. 1998; Nakamura et al. 2001; Cano 2013)

3. GRB 130215A

GRB 130215A was detected at 01:31:30 UT on 15-February-2013 by the *Swift*-BAT, and has a $T_{90} = 65.7 \pm 10.8$ s in the 15–350 keV energy range (D'Elia et al. 2013; Barthelmy et al. 2013a). Due to a Moon observing constraint, *Swift* could not slew to the BAT position, thus there are no XRT or UVOT data for this GRB. The burst was also observed by *Fermi*-GBM (Younes & Bhat, 2013) with $T_{90} \approx 140$ s in the 50–300 keV energy range; and by the Sukaku Wide-Band All-sky Monitor (WAM) with $T_{90} \approx 46$ s in the 100–1000 keV energy range (Ishida et al. 2013). Rapid follow-up observations were performed by many ground-based telescopes (Zheng et al. 2013a, 2013b; LaCluyze et al. 2013; Cenko, 2013; Covino et al. 2013; Butler et al. 2013a, 2013b; Gendre et al. 2013; Xu & Zhang, 2013; Hentunen et al. 2013a; Zhao & Bai, 2013; Wren et al. 2013; Kuroda et al. 2013; Knust et al. 2013; Perley, 2013a, 2013b; Singer et al. 2013). The redshift was measured to be $z = 0.597$ (Cucchiara et al. 2013). The AG was clearly detected at 93 GHz at +2.73 hr (Perley & Keating 2013). A spectrum of SN 2013ez was obtained with the GTC (de Ugarte Postigo et al. 2013a, 2013b). An estimate of the isotropic energy release in γ-rays ($1 - 10^4$ keV, rest-frame) is $E_{\rm iso,\gamma} = 3.1^{+0.9}_{-1.6} \times 10^{52}$ erg[5]. The probability that GRB 130215A arises from a collapsar (Bromberg et al. 2013) based on T_{90} alone is $99.995 \pm 0.002\%$ (BAT) and $99.487 \pm 0.358\%$ (GBM). We have used a foreground extinction value of $E(B-V)_{\rm fore} = 0.162$ mag (Schlegel et al. 1998) for GRB 130215A.

3.1. Data Reduction, Photometry & Spectroscopy

We obtained observations with several ground-based telescopes. ROTSE-III automatically starting imaging the field of GRB 130215A 697 s after the initial γ-ray trigger, locating a new, bright (unfiltered=14.2) source at 02:54:00.7 +13:23:43.7 (J2000), with an uncertainty of $< 1''$. Further observations were obtained during the first day with the Nordic Optical Telescope (NOT) and the Gamma-Ray burst Optical/Near-Infrared Detector (GROND; Greiner et al. 2008). Several hours of observations were obtained with the Reionization and Transients Infrared Camera (RATIR[6]) on the 1.5-m Harold Johnson Telescope at the Observatorio Astronómico Nacional on Sierra San Pedro Mártir during the first few hours after the trigger, with additional epochs at $t - t_0$ =2,3,4,8,11,17 d. We also obtained two epochs of spectroscopy and one epoch of optical photometry with the GTC. Early spectroscopy of the AG was performed with OSIRIS, $t - t_0 = 0.79$ d after the GRB using the R1000B grism, which gives a spectral resolution of $\delta\lambda/\lambda \sim 1000$ and a coverage from 3600 to 7500 Å. We obtained an additional spectrum of the accompanying SN 2013ez at $t - t_0 = 25.78$ d, the timing of which was planned to observe the SN at or near maximum light. This observation was performed using the R500R grism, with a spectral resolution of $\delta\lambda/\lambda \sim 600$ and coverage from 4800 to 10000 Å. Each spectrum was reduced using standard techniques with IRAF-based scripts. Late time images ($t - t_0 = 372.8$ d) of the GRB field were obtained with the GTC in filters gri, while a late epoch ($t - t_0 = 331.8$ d) was obtained with the 3.5-m CAHA telescope in J.

The optical data were calibrated via standard star photometry. On 21-August-2013 GROND obtained images of the GRB field and an SDSS (Abazajian et al. 2009) field located at 03:00:48.0, +19:57:00 (J2000), with the SDSS field taken immediately after the GRB field. Both sets of images were taken under photometric conditions. The calibration was performed using a zeropoint and an airmass correction, and the solution was used to calibrate a set of secondary standards in the field of the GRB. Each datatset was then calibrated to a subset of these stars, depending which ones were in the field of view of each telescope. A summary of our photometry is presented in Table 6.

3.2. The Afterglow

Figure 4 displays our optical photometry, which has been corrected for foreground extinction and then converted into monochromatic fluxes. The LCs were simultaneously fit with a single PL up to $t - t_0 = 1.0$ d (except the Y-band data, which were normalised using the detection at 2.5 d, and is likely over-estimated in brightness as this detection appears to be during the plateau phase), with the best-fitting value of the temporal index being $\alpha = -1.25 \pm 0.01$ ($\chi^2/dof = 231.9/141$). After one day the LCs deviate away from the PL-like decline and undergo a plateau phase that lasts up to six days post burst. The LCs then "break" again before leveling out a further time due to light coming from SN 2013ez.

Due to the lack of XRT data we have not been able to construct an X-ray to optical energy spectrum. Instead we have used our contemporaneous optical/NIR data taken with RATIR and GROND over several epochs to get an estimate of the rest-frame

[5] http://butler.lab.asu.edu/swift/bat_spec_table.html

[6] www.ratir.org

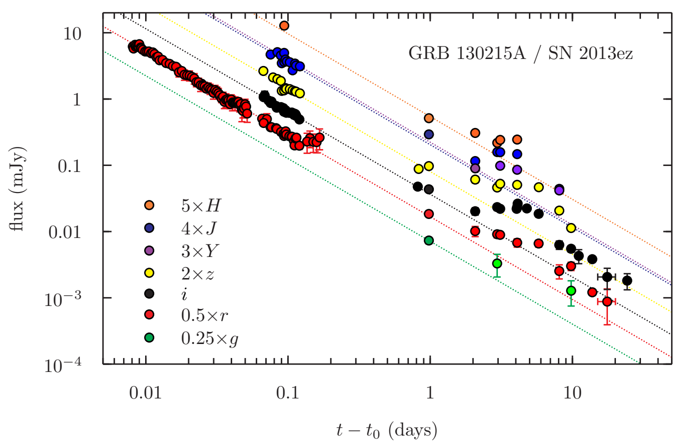

Fig. 4. GRB 130215A: Optical and NIR LCs. The optical data have been corrected for foreground extinction and converted into mJy using the flux zeropoints from Fukugita et al. (1995). All filters have been fit with a single PL up to $t - t_0 = 1.0$ d (except Y which was normalised using the detection at 2.5 d), where $\alpha = -1.25 \pm 0.01$ ($\chi^2/dof = 231.9/141$). A "plateau" is seen in all filters from $t - t_0$ =1–6 d, where each LC deviates away from a single PL-like decline.

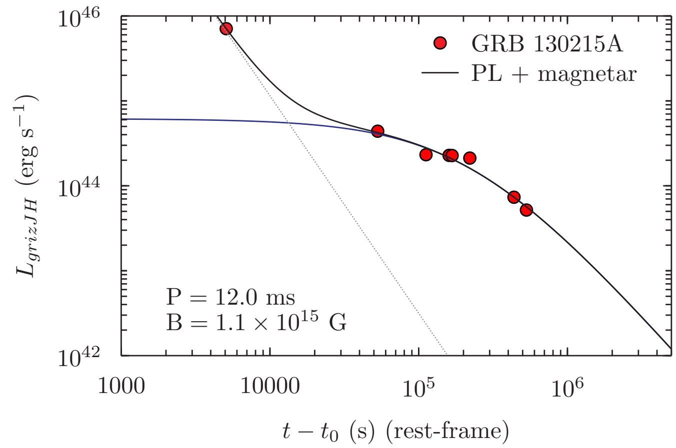

Fig. 5. GRB 130215A: Rest-frame bolometric LC created from our *grizJH* observations. The analytical model from Zhang & Mészáros (2001; see also Rowlinson et al. 2013) has been fit to the LC, which considers energy injection from a millisecond magnetar (plateau and late decline) added to an initial PL-like decline. From the model we find an initial spin period of $P_0 = 12.0$ ms, a magnetic field strength of $B = 1.1 \times 10^{15}$ G, a plateau luminosity of $L_{plat} = 6.1 \times 10^{44}$ erg s^{-1} and a rest-frame plateau duration of $T_{plat} = 2.3 \times 10^5$ s. Encouragingly, the values of the initial spin period and *B*-field are *realistic*, and are loosely similar to those found for long-duration GRBs 060729 and 130427 (see the main text), as well as the sample of short-duration GRBs in Rowlinson et al. (2013).

extinction. Using the same epochs as those used to construct the bolometric LC in Section 3.3, we have fit the empirical extinction curves of the SMC, LMC and MW from Pei (1992), using a method similar to Kann et al. (2006) and Kann et al. (2010). Each SED is well described by a single PL, with very little if any curvature, implying there is no need to invoke the presence of rest-frame dust extinction. Each epoch is equally well fit by each dust-extinction template. Indeed some epochs predict a (very small) negative value for the extinction, which is an unphysical conclusion, while the other epochs are consistent with zero rest-frame extinction. Throughout the rest of the analysis of GRB 130215A, we assume $E(B-V)_{\rm rest} = 0.0$ mag.

3.3. Magnetar Origins?

There are many examples of GRB LCs that show deviations away from a PL-like decay, e.g. GRB 011211 (Jakobsson et al. 2003), GRB 021004 (de Ugarte Postigo et al. 2005), GRB 030429 (Jakobsson et al. 2004), GRB 060526 (Thöne et al. 2010), GRB 090926A (Rau et al. 2010; Cenko et al. 2011) and GRB 100814A (de Pasquale et al. 2013; Nardini et al. 2014). One is also reminded of the peculiar LC of GRB 030329 (Matheson et al. 2003) that displayed very complex behaviour and complicated the decomposition of the SN light from the LC. So while the AG LCs of some GRB-SNe are rather smooth (e.g. GRB 090618, Cano et al. 2011a), others are very complex.

The term "energy injection" is used to explain these peculiar bumps, flares and plateaus, where extra energy is pumped into the FS, causing the AG to become brighter (e.g. Panaitescu et al. 1998; Rees & Mészáros 1998; Kumar & Piran 2000; Sari & Mészáros 2000). Energy injection can arise from different physical sources including Poynting flux emitted by a central engine (e.g. Usov 1992; Dai & Lu 1998), the collision of additional shells of material that collide with the original shells that generated the initial γ-ray burst (Zhang et al. 2006); a reverse shock (RS) created from the collision and pile up of multiple shells with the original shells (e.g. Sari & Mészáros 2000; Kobayashi 2000; Harrison & Kobayashi 2013; Japelj et al. 2014); a two-component jet (Granot et al. 2005) where a rebrightening in the optical bands can arise due to emission from a narrow jet seen off-axis; or a combination of forward and reverse shocks (de Pasquale et al. 2013) including the "thick-shell" scenario, where a combination of the forward and reverse shock (the latter is relativistic) leads to a plateau phase in the observations (Leventis et al. 2014) . A more exotic source of energy injection can arise from a quark nova (Staff et al. 2008). During the transition of the newly formed compact object from neutron star→quark star→black hole, accretion onto the quark star produces a source of extra energy that can be pumped into the ejecta, which can account for the prompt emission as well as flares and plateaus in X-ray LCs. However, injection from an accreting quark star cannot explain plateaus in optical/NIR LCs. One key idea that all these models have in common is that the later the energy injection episode, that much more energy is required to create bumps and plateaus of similar magnitude.

Another source of energy injection into the FS can arise from a millisecond magnetar central engine, which deposits Poynting flux dominated dipole radiation into the ejecta (e.g. Zhang & Mészáros 2001; Dall'Osso et al. 2011). The millisecond magnetar model has been considered as a plausible source of energy injection for GRBs, with some notable examples being GRB 000301C (Zhang & Mészáros 2001), GRB 060729 (Xu et al. 2009; Dall'Osso et al. 2011; Lü & Zhang 2014), GRB 120326A (Hou et al. 2014) and GRB 130427A (Bernardini et al. 2014). In these investigations plateau phases in the X-ray LCs are attributed to extra energy arising from a millisecond magnetar, where energy injection "refreshes" the FS. This is in contrast to the analysis of GRB 070110 (Troja et al. 2007) and the recent study of a sample of short GRBs by Rowlinson et al. (2013), where both authors attribute the plateaus in the X-ray LCs as flux coming *directly* from the millisecond magnetar.

To our knowledge, to date no attempt has been made to constrain the behaviour of a possible magnetar central engine using a bolometric LC of the AG constructed from optical/NIR observations. Predominantly bolometric X-ray modelling has been the status quo, though an estimate of the optical contribution (R-band) was made for GRB 130427A by Bernardini et al. (2014) and R-band data of GRB 120326A (Hou et al. 2014). In this work we are able to fully exploit the wide filter coverage and simultaneous observations obtained by both GROND and RATIR to create a bolometric LC in the filter range $grizJH$ (observer frame) with the aim of determining whether energy injection from a magnetar central engine provides a plausible explanation for the plateaus seen in the optical/NIR LCs. We have used data from a total of eight epochs (ranging from $t - t_0 = 0.1$–9.8 d in the observer frame); i.e. before the period where the SN starts to dominate the LCs). We have followed a standard method to construct our bolometric LC (e.g. Cano et al. 2014), taking the following steps: (1) correct all magnitudes for foreground and rest-frame extinction, (2) convert magnitudes into monochromatic fluxes using flux zeropoints in Fukugita et al. (1995). For epochs where there are not contemporaneous observations, we have linearly interpolated the flux LCs and SEDs to estimate the missing flux. Then, for each epoch of multi-band observations, and using the effective wavelengths from Fukugita et al. (1995) we: (3) interpolate (linearly) between each datapoint, then (4) integrate the SED over frequency, assuming zero flux at the integration limits, and finally (5) correct for "filter overlap". The linear interpolation and integration were performed using a program written in Pyxplot. The resultant LC is shown in Figure 5.

We have made similar assumptions as Rowlinson et al. (2013), namely that the magnetar mass is 1.4 $M_{\odot}$ and the radius is 10^6 cm, which allows us to reduce the number of free parameters in the fit. The final fit is a combination of an initial PL added to the magnetar model:

$$L_{magnetar}(t) = L_0 \left(1 + \frac{t}{T_0}\right)^2 + \Lambda t^{-\alpha} \qquad (1)$$

where L_0 is the plateau luminosity, T_0 is the plateau duration, and Λ is the normalisation constant for the PL. The values of L_0 and T_0 can be related back to equations 6 and 8 in Zhang & Mészáros (2001; see as well Rowlinson et al. 2013) to estimate the initial spin period and magnetic field strength of the magnetar. Fitting this model to our rest-frame bolometric LC, we find an initial spin period of $P_0 = 12.0$ ms, a magnetic field strength of $B = 1.1 \times 10^{15}$ G, a plateau luminosity of $L_0 = 6.1 \times 10^{44}$ erg s^{-1}, a rest-frame plateau duration of $T_{plat} = 2.3 \times 10^5$ s, and $\alpha = -2.6 \pm 0.7$.

Encouragingly, the values of the initial spin and magnetic field are *realistic*, and are found to be comparable to those found for other GRBs with associated SNe: (1) GRB 060729: $P = 1.5$ ms and $B = 0.27 \times 10^{15}$ G (Xu et al. 2009); $P = 2.0$ ms and $B = 3.2 \times 10^{15}$ G (Dall'Osso et al. 2011); and $P = 1.5$ ms and $B = 0.25 \times 10^{15}$ G (Lu & Zhang 2014); (2) GRB 130427A: $P \sim 20$ ms and $B \sim 10^{16}$ G (Bernardini et al. 2014). The spin period determined from observations of GRB 130215A falls within the estimates for GRBs 060729 and 130427A, while the magnetic field strengths vary by two orders of magnitudes for these three events. Moreover, these values are fully consistent with the values determined for a sample of short GRBs by Rowlinson et al. (2013), and for short GRB 130603B (de Ugarte Postigo et al. 2013c). Further discussion on the plausibility of energy injection arising from a millisecond magnetar is presented in Section 5.

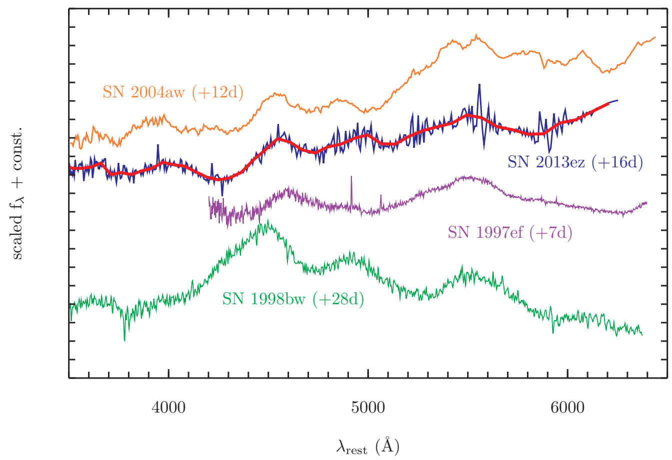

Fig. 6. GRB 130215A / SN 2013ez: SN+host+AG (blue) rest-frame spectra (wavelength in air). The SN spectrum was taken at $t - t_0 = 25.8$ d (16.1 d rest-frame). The red line is the SN spectrum binned by a factor of 10 to assist in identifying the main absorption features in the spectrum. Plotted for comparison are the spectra of SN 1998bw (green; GRB-SN) at +28 d from peak B-band light, SN 1997ef (Ic-BL; purple) at +7 d, and SN 2004aw (Ic; orange) at +12 d, all of which have been arbitrarily transformed in flux in order to provide a good visual comparison. The absorption feature seen at ~5100 Å in the spectrum of SN 2013ez is thought to blueshifted Fe II λ5169 at $\approx$ 4000 km s^{-1}.

3.4. The Host Galaxy

We re-observed the field of GRB 130215A on 22-February-2014 with the GTC telescope in filters gri. The host galaxy is not visible in any of our co-added images. We derive 3-σ upper limits for an isolated point source in our images of: $g > 26.2$, $r > 26.1$, $i > 25.1$, which are not corrected for foreground extinction. We also obtained a late-time J-band image with the 3.5-m CAHA telescope on 12-January-2014, where again no object is detected at the position of the GRB. We derive upper limits of $J > 23.2$.

At $z = 0.597$, and a distance modulus of $\mu = 42.72$, these upper limits imply observer-frame, absolute magnitude limits of the host galaxy of $M_g > -16.5$, $M_r > -16.6$, $M_i > -17.6$ and $M_J > -19.5$.

3.5. The Supernova

Figure 6 shows the spectrum (blue) obtained with the GTC of SN 2013ez (+host) at $t - t_0 = 25.8$ d. We have binned the spectrum by a factor of 10 (where the original resolution is 9.76 Å pixel^{-1}) to aid clarity (red). Clear undulations are seen in the spectrum that are reminiscent of SNe Ic and Ic-BL. Prominent absorption features are seen near $\lambda \approx 4200$, 4700, 5100 and 5800 Å. Plotted for comparison are the spectra of SN 1998bw (green) from 8-June-1998 (+28 days from peak B-band light; Patat et al. 2001); SN 1997ef (Ic-BL; purple) from 17-December-1997 (+7 d; Garnavich et al. 1997; Hu et al. 1997); and 2004aw (Ic) from 07-Apr-2004 (+12 d; Taubenburger et al. 2006). The spectra have been arbitrarily shifted in flux to provide a good visual comparison with SN 2013ez. Both SN 1997ef and SN 2004aw provide a good visual fit to the spectrum of 2013ez (SNID; Blondin & Tonry 2007 also chooses SN 1997ef as the best-fitting template at a redshift of $z = 0.602$).

Upon comparison with the other spectra, the absorption feature near 5100 Å is thought to be blueshifted Fe II λ5169. We

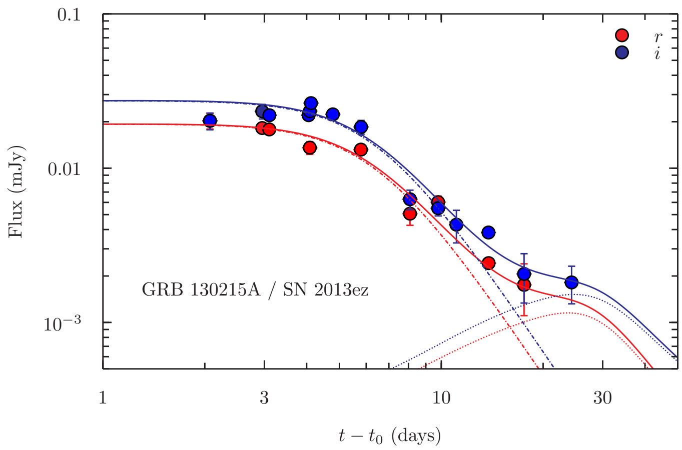

Fig. 7. GRB 130215A / SN 2013ez: Optical LCs in r (red) and i (blue). The AG (dot-dashed) and SN (dotted) components are shown in the same colour as their corresponding filter, while the solid lines are the sum of both components. Data at times > +2 d have been fit with a broken PL consisting of a plateau phase and a break to a steeper decay phase, where we have assumed that the time that the LC breaks and the decay rate after the break are the same in both filters. The best-fitting values (for magnitudes that are not "host-subtracted", see the main text) are: $\alpha_2 = -3.28 \pm 0.25$ and $T_B = 6.39 \pm 0.35$ d. Due to the (1) lack of host detection in our deep GTC images, and (2) lack of datapoints at times when the SN is the dominant source of flux we have not been able to precisely constrain the SN's properties. When we consider the two extremes of the host brightness (see main text), we constrain the luminosity factor of SN 2013ez to be $0.6 \leq k \leq 0.75$.

fit a single Gaussian to this feature in our binned spectrum to determine the minimum wavelength of the line profile using the method presented in Cano et al. (2014). We modelled several spectra of different bin sizes in order to get an estimate of the uncertainity of the minimum of the Gaussian, finding it to be between $5090 \leq \lambda_0 \leq 5110$ Å, which corresponds to a blueshifted velocity of $-4620 \leq v \leq -3440$ km s^{-1}. This velocity is smaller than seen for other GRB-SNe, where velocities of order 10,000 km s^{-1} or greater are seen at times only a few days from peak light (e.g. Fig. 5 in Schulze et al. 2014). This implies that SN 2013ez is of a type Ic rather than Ic-BL, though we must consider that the spectrum is of relatively low S/N when making this conclusion.

Further supporting the slow ejecta velocity of SN 2013ez at this epoch are the line and photospheric velocities determined for the comparison SNe. Iwamoto et al. (2000) and Mazzali et al. (2000) find the velocity of the Si II λ6355 in the 17-December spectrum of SN 1997ef to be ≈ -8000 km s^{-1}, while the photospheric velocity used in the synthetic spectrum of Mazzali et al. (2000) is ≈ 7500 km s^{-1}. Similarly, Patat et al. (2001) measured the blueshifted velocity of the Si II λ6355 in their 8-June spectrum to also be ≈ -8000 km s^{-1}. Moreover, Taubenburger et al. (2006) measure the blueshifted velocity of the Si II λ6355 to be $\approx$7000–8000 km s^{-1} in the spectrum from 07-Apr-2004. We note that while our spectrum of SN 2013ez does not stretch far enough into the red to detect any possible Si II λ6355 absorption, the comparison is quite useful none the less.

While the identification of SN 2013ez is unambiguous, the plateau in the optical/NIR complicates our ambition of decomposing the LCs in order to isolate the SN contribution. The situation is also perplexed by the paltriness of photometric observations of SN 2013ez near peak. Nevertheless we have attempted to decompose the optical LCs to estimate the brightness of SN 2013ez in filters r and i (Fig. 7). We have fit a broken PL to the LCs, and imposed a plateau phase ($\alpha_1 = 0.01$), that then breaks at some time (T_B) to a steeper decay phase (α_2). We have assumed that the time the LC breaks and the rate of decay after the break are the same in both filters, and these two parameters are allowed to vary during the fit.

The decomposition is further complicated by the fact we have not detected the host in our deep GTC images (see section 3.4), we must consider two scenarios: (1) magnitudes that are not "host-subtracted", and (2) take the host brightness equal to the limits obtained from the GTC images (and correct for foreground extinction). These two scenarios can be considered to be the two extremes to the SN brightness, for certainly the host will be contributing *some* flux, but no more than the upper limits of the GTC images.

In scenario (1) we find best-fitting AG parameters of $\alpha_2 = -3.28 \pm 0.25$ and $T_B = 6.39 \pm 0.35$ d, while in scenario (2) we find $\alpha_2 = -3.44 \pm 0.28$ and $T_B = 6.41 \pm 0.34$ d. Unsurprisingly the time the LC breaks is essentially the same in both scenarios, while the LCs decay faster when we remove a host contribution. We also note that the break-time is later than that found in the magnetar model ($T_{\rm B} = 4.3$ d in observer frame). As for GRB 120729A, we have had to fix the stretch factor to $s = 1.0$ due to the lack of datapoints. In scenario (1) we find $k \approx 0.75$, while in scenario (2) we find $k \approx 0.6$. These two values can be considered the upper and lower limits to the brightness of SN 2013ez in these filters. Taking these values at face value implies peak brightnesses of $M_r = -18.7$ to -19.0, and $M_i = -19.0$ to -19.3. Again, there is little merit in estimating the peak times due to the unknown stretch values. Finally, using the method in C13, we estimate a nickel mass in the range $0.25 \leq M_{\rm Ni} \leq 0.30\ M_\odot$.

4. GRB 130831A

GRB 130831A was detected at 13:04:16 UT on 31-August-2013 by the *Swift* Burst Alert Telescope (BAT), and has a $T_{90} = 32.5 \pm 2.5$ s in the 15–350 keV energy range (Hagen et al. 2013; Barthelmy et al. 2013b). It was also detected by Konus-Wind (Golenetskii et al. 2013), who estimate an isotropic energy release in γ-rays of $E_{\rm iso,\gamma} = 4.6 \pm 0.2 \times 10^{51}$ erg in the 20 keV–15 MeV range. The probability that GRB 130831A arises from a collapsar (Bromberg et al. 2013) based on T_{90} alone is $99.969 \pm 0.006\%$ (BAT).

Rapid follow-up of GRB 130831A was performed by several ground-based telescopes (Guidorzi & Melandri 2013; Xu et al. 2013b; Yoshii et al. 2013; Xin et al. 2013; Trotter et al. 2013; Leonini et al. 2013; Masi & Nocentini 2013; Izzo & D'Avino 2013; Hentunen et al. 2013b; Sonbas et al. 2013; Butler et al. 2013c; Chester & Hagen 2013; Volnova et al. 2013a, 2013b, 2013c, 2013d; Pozanenko et al. 2013 and Khorunzhev et al. 2013). The AG was not detected at radio (Laskar et al. 2013) or sub-mm wavelengths (Zauderer et al. 2013; Smith et al. 2013). A redshift of $z = 0.479$ was measured with Gemini-North (Cucchiara & Perley 2013). A spectrum of the associated supernova, SN 2013fu, was obtained with the VLT by Klose et al. (2013), with additional spectra reported in Nicuesa Guelbenzu et al. (2013). We have used a foreground extinction value of $E(B-V)_{\rm fore} = 0.046$ mag (Schlegel et al. 1998) for GRB 130831A.

4.1. Data Reduction & Photometry

We obtained optical observations with several ground-based telescopes. The 0.65-m SANTEL-650 and 0.5-m VT-50 telescopes of the UAFO/ISON-Ussuriysk started imaging (unfiltered) the GRB field just over 10 minutes after the initial trigger, obtaining nearly consecutive images for six straight hours. Additional follow-up observations were obtained with the Gissar observatory 0.7-m telescope, the 0.4-m SANTEL-400AN telescope (UAFO/ISON-Ussuriysk observatory), the 0.7-m AZT-8 telescope operated by the Institute of Astronomy, Kharkiv National University and the 1.5-m AZT-22 telescope at Maidanak observatory. Data obtained at times $t - t_0 < 2.0$ d with aforementioned Russian telescopes are presented in de Pasquale et al. (2014, in prep), while everything at this time and later are presented in this paper. We obtained several epochs of photometry with the 2.5-m NOT, three epoch with the 4.2-m William Hershel telescope (WHT), and four epochs with the 2.0-m LT. We also obtained a single late-time epoch with the Gemini Multi-Object Spectrograph (GMOS; Hook et al. 2004) mounted at Gemini-South as a part of the program GS-2013B-Q-69. The data were reduced in a standard fashion with the Gemini IRAF software package for GMOS (v1.12).

The optical data were calibrated using SDSS stars in the GRB field with a zeropoint between the instrumental and catalog magnitudes. Observations obtained with each Russian telescope in Johnson/Cousins filters BVR_cI_c were calibrated by converting the SDSS (AB) magnitudes of local standards into Johnson/Cousins (Vega) using transformation equations in Lupton (2005)[7]. The late-time r observations taken with the NOT, WHT and Gemini were converted into R_c using transformation equations from Jordi et al. (2006), which require a colour term $(r - i)$ in the calculations. In an identical procedure as for GRB 120729A (see section 2.1) we interpolated the i LC to the times of the r LC, extracting the i magnitude. A summary of our photometry is presented in Table 6.

4.2. The Afterglow

Our R_ciz optical data are displayed in Fig. 9. All magnitudes are corrected for foreground and rest-frame extinction. We have "host-subtracted" the optical data in R_c and i using the host detections (see Section 4.4) in the same filters, and then converting all magnitudes into monochromatic fluxes and then mathematically subtracting the host flux from the earlier epochs. The z data have not been host-subtracted due to lack of observations of the host in z at late times. All LCs are well described by a single PL, where we have assumed that the LCs decay at the same rate in all filters, where $\alpha = -1.63 \pm 0.02$. We note the presence of a "bump" or short plateau phase in the R-band LC between $t - t_0 \sim 3$–5 d, however this short phase does not appear to affect our analysis of the decay rate and subsequent optical properties of the SN in R_c and i.

4.3. The Spectral Energy Distribution

In an identical analysis as Section 2.3 we have constructed rest-frame X-ray to optical SEDs in order to get an estimate of the rest-frame extinction (Fig. 8). We have fit two epochs of data at $t - t_0 = 0.39$ d and 1.12 d (observer frame), taken with the NOT and MAO respectively. The optical data have been corrected for foreground extinction.

[7] http://www.sdss.org/dr4/algorithms/sdssUBVRITransform.html

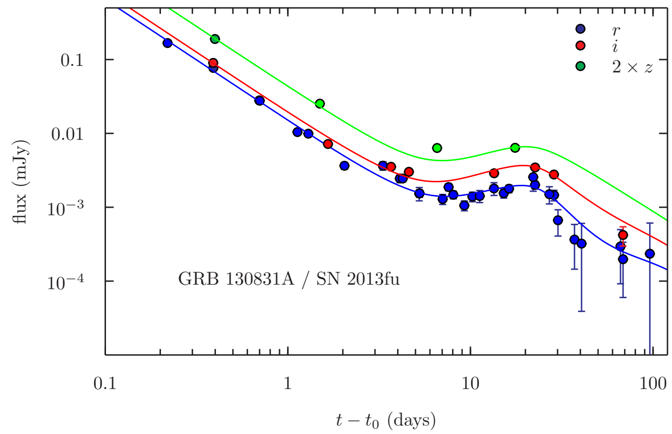

Fig. 9. GRB 130831A: Optical (R_ciz) light curves. The solid lines in each filter are the sum of the AG and SN components. The optical data have been corrected for foreground extinction, and the R_c and i are "host-subtracted" (see the text). The z data have not been host-subtracted due to lack of observations of the host in z at late times. All LCs are well fit with a single PL, where we have assumed that the LCs decay at the same rate in all filters, where $\alpha = -1.63 \pm 0.02$. A clear SN bump is seen in R_c and i, and a flattening of the LC is seen in z, which can be attributed to flux coming from SN 2013fu. In each filter we have simultaneously fit a "SN-component" to determine the stretch (s) and luminosity (k) factors in each filter. Due to the lack of observations in z at late times we have fixed the value of stretch factor to be the same in i and z (i.e. $s_i \equiv s_z$). Our best-fitting parameters are: $k_R = 0.65 \pm 0.03$ and $s_R = 0.82 \pm 0.03$; $k_i = 1.07 \pm 0.05$ and $s_i = 0.88 \pm 0.03$; $k_z = 1.00 \pm 0.19$ and $s_z = s_i = 0.88$ (fixed). As the z data are not host-subtracted, the luminosity factor is an upper limit to the maximum brightness of SN 2013fu in this filter.

As before both single and broken PLs were fit to the SEDs, and we find that for both epochs a single PL fits the data well. Our results for both epochs are: (1) $t - t_0 = 0.39$ d ($\chi^2/dof = 49.2/45$): $\beta = 0.85 \pm 0.01$, $A_V < 0.1$ mag (90% CL), and $N_{\rm H} = 4.2 \pm 0.8 \times 10^{20}$ cm^{-2}; (2) $t - t_0 = 1.12$ d ($\chi^2/dof = 42.0/45$): $\beta = 0.75 \pm 0.06$, $A_V = 0.21^{+0.28}_{-0.21}$ mag, and an intrinsic column density of $N_{\rm H} = 3.5 \pm 1.0 \times 10^{20}$ cm^{-2}. We thus conclude that the extinction local to GRB 130831A is consistent with being zero, and for our analysis we use the value of $E(B - V)_{\rm rest} = 0.0$ mag.

4.4. The Host Galaxy

We observed the field of GRB 130831A at late times with the LT (i) and NOT (r), where an extended object is visible at the GRB position in both images, which we attribute as the host galaxy. In the I-band LT image taken on 05-Jan-2014 at $t - t_0 = 127.3$ d (+86.1 d in rest-frame), we measure $i = 24.23 \pm 0.10$. In our R-band NOT image taken on 03-Feb-2014 at $t - t_0 = 156.3$ d (+105.7 d in rest-frame), we measure $r = 24.06 \pm 0.09$. These magnitudes are not corrected for foreground extinction. In terms of absolute magnitude, we find (observer-frame) $M_r = -18.06 \pm 0.09$ and $M_i = -17.89 \pm 0.10$. The colour $r - i = -0.17$ suggests that the host galaxy is rather blue. We note that we did not attempt to fit galaxy SEDs due to the spareness of host observations.

4.5. The Supernova

Clear SN bumps are seen in Fig. 9, which are particularly pronounced in the well-sampled R-band LC, and also seen in i,

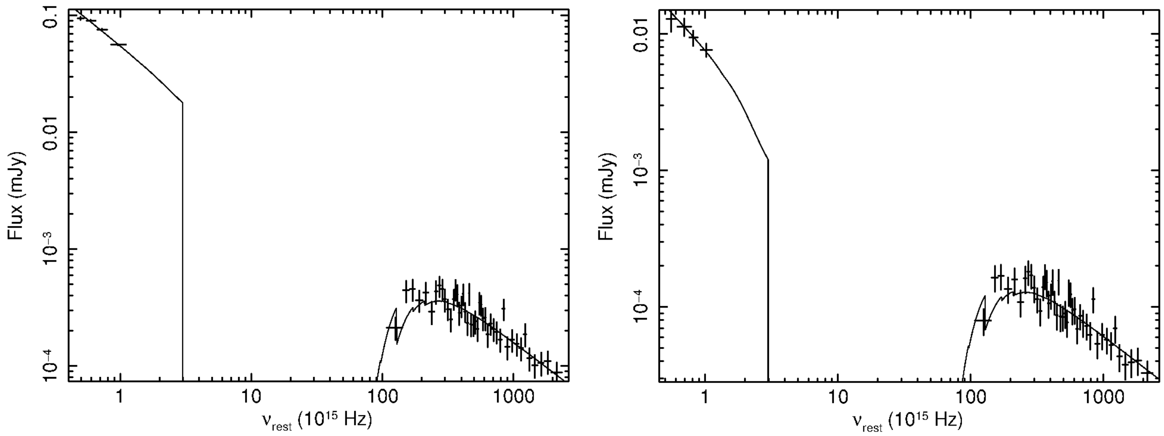

Fig. 8. GRB 130831A: X-ray to optical SED of the AG at $t - t_0 = 0.39$ and 1.12 d (observer frame). It is found that a single PL provides a good fit to both epochs of data ($\beta = 0.85 \pm 0.01$ and 0.75 ± 0.06 respectively). For the first epoch (left) we find $A_V < 0.1$ mag (90% CL), while in the second epoch we find $A_V = 0.21^{+0.28}_{-0.21}$ mag. The results of the SED fitting indicate that the rest-frame extinction is consistent with being $E(B-V) = 0.0$ mag. Additionally we find the intrinsic column density to be $N_{\rm H} \approx 3 - 4 \times 10^{20}$ cm^{-2} for both epochs.

and to a lesser extent in z, where a flattening of the LC is seen, which can be attributed to flux coming from SN 2013fu. When fitting the optical data in Section 4.2 we have simultaneously fit a "SN-component" to determine the stretch (s) and luminosity (k) factors in each filter. Our best-fitting parameters are: $k_R = 0.65 \pm 0.03$ and $s_R = 0.82 \pm 0.03$ $k_i = 1.07 \pm 0.05$ and $s_i = 0.88 \pm 0.03$; $k_z = 1.00 \pm 0.19$ and $s_z = s_i = 0.88$ (fixed). Due to the lack of observations in z at late times we have fixed the value of s to be the same as in i. Moreover, as the z data are not host-subtracted, the luminosity factor is an upper limit to the maximum brightness of SN 2013fu in this filter.

We have determined the peak absolute magnitude, and time of peak light, of SN 2013fu in each filter. In R_c: $M_R = -18.89 \pm 0.05$ and $t_p = 18.16 \pm 0.66$ d (12.28 ± 0.44 d in rest frame); i: $M_i = -19.59 \pm 0.05$ and $t_p = 20.13 \pm 0.069$ d (13.61 ± 0.47 d in rest frame); z: $M_z = -19.45 \pm 0.19$ and $t_p \approx 20.8$ d (≈ 14.1 d in rest frame). The peak time in z is tentative however, given that we have no been able to directly determine the stretch factor directly from our observations. At $z = 0.479$, observer-frame i ($\lambda_{\rm eff} = 7706$ Å) is roughly rest-frame V ($\lambda_{\rm eff} = 5505$ Å): $7706/1.4791 = 5210$ Å. Making a k-correction using the formulation of Hogg et al. (2002), and a spectrum of SN 1998bw as a template, we find a k-correction from observer-frame i to rest-frame V of $k_{i \rightarrow V} \approx 0.25$ mag. This implies a rest-frame, peak magnitude of $M_V \approx -19.34$. This value is consistent with the average peak V-band magnitude found for a sample of k-corrected LCs of GRB-SNe analysed by Richardson (2009), who found $M_{V,\rm peak} = -19.2 \pm 0.2$ (standard deviation of $\sigma = 0.7$ mag).

It is seen that in the well-sampled R-band LC that the SN appears to decrease in brightness faster than the k-corrected LC of SN 1998bw. There is also a hint of this in the I-band LC, though we cannot draw many conclusions based on a single datapoint at late times. When we calculate Δm_{15} in R_c (where Δm_{15} is the amount the LC fades from peak light to 15 days later; here we have computed this for rest-frame times) for SN 2013fu and SN 1998bw, (where the latter is transformed by $k_R = 0.65 \pm 0.03$ and $s_R = 0.82 \pm 0.03$), we find $\Delta m_{15} \approx +1.99$ and $\Delta m_{15} \approx +1.45$ respectively. This clearly shows that 2013fu evolves faster than the archetype GRB-SN 1998bw. Therefore, in this case the shape of the template SN does not provide the best description for the temporal evolution of SN 2013fu. This type of behaviour has been seen for other GRB-SNe, such as SN 2010dh associated with XRF 100316D (Cano et al. 2011), SN 2006aj associated with XRF 060218 (Ferrera et al. 2006), as well local SNe Ibc presented in C13.

Using the model in C13 we have estimated the nickel mass, ejecta mass and kinetic energy of SN 2013fu. Without knowledge of the peak photospheric velocity of SN 2013fu, we have used the average peak photospheric velocity determined by C13 for a sample of GRB-SNe: $v_{ph} = 20 \pm 2.5 \times 10^3$ km s^{-1}. To estimate the nickel mass we have computed the average luminosity factor from the r and i filters (neglecting the z observation as it is not host subtracted and is therefore an overestimate of the SN's brightness), $\bar{k} = 0.86 \pm 0.21$. We have estimated the ejecta velocity using the peak photospheric velocity and an average of the stretch factor in R and i, $\bar{s} = 0.85 \pm 0.03$. We find bolometric properties of: $M_{\rm Ni} = 0.31 \pm 0.09$ $M_\odot$, $M_{\rm ej} = 5.08^{+1.18}_{-0.55}$ $M_\odot$ and $E_{\rm K} = 2.02^{+1.13}_{-0.64} \times 10^{52}$ ergs. The uncertainties in the ejecta mass and kinetic energy arise from the uncertainties in the stretch and luminosity factors as well as the spread of peak ejecta velocities around the mean value in C13.

5. Discussion & Conclusions

5.1. The Supernovae

We have presented optical/NIR photometry for three GRB-SNe, and a spectrum of SN 2013ez that was associated with GRB 130215A. For each SN we have attempted to derive their luminosity factor (k), and the stretch factor (s) of SN 2013fu relative to a template supernova (SN 1998bw), which has been redshifted/k-corrected to that of each GRB-SN considered here. We have also estimated the peak, observer-frame magnitude of each SN in every available filter, as well as the time of peak light for SN 2013fu.

When analysing the optical properties of SN 2013fu we found that it is brighter in the redder filters: $k_R = 0.65 \pm 0.03$, $k_i = 1.07 \pm 0.05$ and $k_z = 1.00 \pm 0.19$. The red colour of 2013fu suggests that there is a suppression of flux in observer-frame R-band ($\approx B$-band in rest-frame, e.g. $\lambda_{\rm eff} = 6588/1 + z \approx 4500$ Å) due to metal line blanketing. Line blanketing by Fe II and Ti II, which suppresses flux blueward of ~ 4000 Å, was observed for Type Ib SN 1999dn (Branch et al. 2002; Deng et al. 2000; Cano et al. 2014). Flux suppression due to several iron-group elements

Table 2. GRB-SNe: Observational and Physical Properties ($UBVRIJH$ rest-frame wavelength range)

GRB	SN	Filter (obs)	k	s	$T_{\rm peak,obs}$ (d)	$M_{\rm peak,obs}$	$M_{\rm Ni}$ ($M_{\odot}$)	$M_{\rm ej}$ ($M_{\odot}$)†	$E_{\rm K}$ (10^{51} erg)†
120729A	-	r	1.29 ± 0.19	1.0 (fixed)	-	-18.96 ± 0.15	-	-	-
120729A	-	i	0.76 ± 0.11	1.0 (fixed)	-	-19.29 ± 0.15	-	-	-
120729A	-	**average**	1.02 ± 0.26	1.0 (fixed)	-	-	0.42 ± 0.11	-	-
130215A	2013ez	r	$0.6 - 0.75$	1.0 (fixed)	-	-18.7 to -19.0	-	-	-
130215A	2013ez	i	$0.6 - 0.75$	1.0 (fixed)	-	-19.0 to -19.3	-	-	-
130215A	2013ez	**average**	$0.6 - 0.75$	1.0 (fixed)	-	-	$0.25 - 0.30$	-	-
130831A	2013fu	r	0.65 ± 0.03	0.82 ± 0.03	18.16 ± 0.6544	-18.89 ± 0.05	-	-	-
130831A	2013fu	i	1.07 ± 0.05	0.88 ± 0.03	20.13 ± 0.69	-19.59 ± 0.05	-	-	-
130831A	2013fu	z	$1.00 \pm 0.19^{\ddagger}$	0.88 (fixed)	≈ 20.8	-19.45 ± 0.19	-	-	-
130831A	2013fu	**average** (r & i)	0.86 ± 0.21	0.85 ± 0.03	-	-	0.31 ± 0.09	$5.08^{+1.18}_{-0.55}$	$20.2^{+11.3}_{-6.4}$

SN type	$M_{\rm Ni}$ ($M_{\odot}$)	$M_{\rm Ej}$ ($M_{\odot}$)	$E_{\rm K}$ (10^{51} erg)	
Ib	0.16	3.89	2.3	
Ic	0.19	3.40	2.2	**median values from**
Ibc	0.18	3.56	2.2	**C13.**
Ic-BL	0.26	3.90	1.1	
GRB/XRF	0.34	5.91	2.2	

† Ejecta mass and kinetic energy are calculated using the average peak photospheric velocity of $v_{\rm ph} = (20 \pm 2.5) \times 10^3$ km s^{-1} determined for a sample of GRB-SNe in C13.
‡ z observations of GRB 130831A are not host-subtracted, and are not considered when calculating the average luminosity and stretch factors.

was also observed for XRF-SN 2006aj (Sollerman et al. 2006), while metal line blanketing was also suggested by Bloom et al. (1999) to explain the red colour of the SN bump of GRB 980326

For each SN we have used the luminosity factor averaged over all available filters to estimate the amount of nickel nucleosynthesized during the explosion, while for SN 2013fu we have used the well-sampled LCs to estimate the ejecta mass and kinetic energy of the SN. We do not have knowledge of the photospheric velocity of the SN at peak light, which is a necessary ingredient of the Arnett (1982) model to estimate M_{ej} and E_K. Instead we have used the average photospheric velocity for a sample of GRB-SNe presented in C13. A summary of the observational and physical properties of our three GRB-SNe are presented in Table 2.

C13 determined the median bolometric properties of a large sample of GRB-SNe, finding: $M_{\rm Ni} \sim 0.3 - 0.35$ $M_{\odot}$, $M_{\rm ej} \sim 6.0$ $M_{\odot}$ and $E_{\rm K} \sim 2.0 \times 10^{52}$ erg. The nickel masses derived here agree well with the range in C13, while the ejecta mass and kinetic energy of SN 2013fu is similar to those found in C13. In terms of physical properties, the GRB-SNe in this paper are quite typical of other GRB-SNe. In contrast, the nickel masses are much higher than those seen for SNe Ibc that are not associated with GRBs. C13 derived the median nickel masses for the largest sample of SNe Ibc yet considered, finding: SNe Ibc: $M_{\rm Ni} \sim 0.15 - 0.18$ $M_{\odot}$, and Ic-BL: $M_{\rm Ni} \sim 0.25$ $M_{\odot}$. Similarly the ejecta mass and kinetic energy of SN 2013fu is larger than those of the C13 sample of SNe Ibc ($M_{\rm ej} \sim 3.4 - 3.9$ $M_{\odot}$, $E_{\rm K} \sim 0.2 \times 10^{52}$ erg) and Ic-BL ($M_{\rm ej} \sim 3.9$ $M_{\odot}$, $E_{\rm K} \sim 1.0 \times 10^{52}$ erg).

5.2. The magnetar model

In this work we have derived the initial spin period and magnetic field of a possible millisecond magnetar central engine for GRB 130215A from optical/NIR observations. We constructed a bolometric LC from contemporaneous $grizJH$ observations of GRB 130215A and fit it with the model from Zhang & Mészáros (2001; see as well Rowlinson et al. 2013), finding $P_0 = 12.0$ ms, a magnetic field strength of $B = 1.1 \times 10^{15}$ G, a plateau luminosity of $L_{\rm plat} = 6.1 \times 10^{44}$ erg s^{-1} and a plateau duration (rest-frame) of $T_{\rm plat} = 2.1 \times 10^5$ s. These values are realistic, and reminiscent of those found for other long and short GRBs.

We must consider the limitations our data when interpreting this result. The bolometric LC is constructed from observations of the AG+SN+host. In early epochs the AG will dominate, however in the latter two epochs at $t - t_0$ =8.1 and 9.8 d there will be some contribution of flux coming from SN 2013ez. Moreover there will be a constant contribution from the underlying host galaxy in all epochs. However, at early times the host and SN contribute a negligible amount of flux, though as the AG fades the SN becomes the dominant source of flux, which too fades, leaving the host as the only source of emission (this happens only after 100 days or more). In our deep GTC images we have not detected the host to deep limits: $g > 26.2$, $r > 26.1$, $i > 25.1$. If the host had these magnitudes, it would contribute $\sim 3 - 8, 25\%$ flux at $t - t_0 = 9.8, 25$ d respectively. Obviously fainter magnitudes implies less host contribution.

5.3. Future Prospects

As discussed in the introduction, there are now almost a dozen spectroscopically associated GRB-SNe, though only a few have multi-band observations, with NIR observations very lacking except in only the nearest GRB-SNe. The bolometric properties of GRB-SNe have been shown to be statistically different to those of non-GRB SNe Ibc, imply that non-GRB SNe Ibc arise from different physical scenarios than GRB-SNe. Without the possibility of directly detecting the progenitor star of a GRB-SNe, we must infer its properties indirectly via the application of advanced modelling techniques and simulations of the SNe themselves. Analytical models presented in e.g. Drout et al. (2011) and Cano (2013) can go only so far (within a factor of ≈ 2) in providing a clear description of the physical processes occurring during the SN, which themselves are highly dependent on the explosion mechanism and evolutionary stage of the progenitor at the time of explosion.

As such there is still a great need for high quality optical and NIR photometry and spectra of GRB-SNe. These can then be used to constrain the explosion mechanism and physical properties of the progenitor via SN modelling methods, such as Monte Carlo radiative transfer (RT) simulations (e.g. Mazzali & Lucy 1993; Maeda et al. 2006; Kasen et al. 2006). Simple RT simulations such as SYN++ (Thomas et al. 2011) provides a tool to approximately ascertain the chemical properties of the material passing through the photosphere at a given moment in time. These results can then be used as input to a RT simulation. The spectra can then be used in a method such as “abundance tomography”, which has been successfully used for SNe Ia (e.g. Hachinger et al. 2013; Mazzali et al. 2014) to determine the density structure and abundance stratification in the SN ejecta. Massive stars are evolved and then exploded in hydrodynamic computer simulations, with the result being SN ejecta of a specific density structure and abundance stratification that can be directly compared with observations. In this manner a clever observing strategy aimed at obtaining optical and NIR photometry and spectroscopy with 8–10-m class ground telescopes (to obtain rest-frame *BVRI* LCs, and NIR if possible), which are combined with sophisticated simulations will undoubtedly provide deeper insight into the nature of the progenitor stars of GRB-SNe.

6. Acknowledgements

I am very grateful to Max de Pasquale for countless discussions regarding GRB physics, and Antonia Rowlinson for equally stimulating conversations regarding magnetars. I gratefully acknowledge support by a Project Grant from the Icelandic Research Fund.

The Dark Cosmology Centre is funded by the Danish National Research Foundation.

The research activity of AdUP, CT and JG is supported by Spanish research project AYA2012-39362-C02-02.

AdUP acknowledges support by the European Commission under the Marie Curie Career Integration Grant programme (FP7-PEOPLE-2012-CIG 322307).

TK acknowledges support by the European Commission under the Marie Curie Intra-European Fellowship Programme.

Based on observations made with the Nordic Optical Telescope, operated by the Nordic Optical Telescope Scientific Association at the Observatorio del Roque de los Muchachos, La Palma, Spain, of the Instituto de Astrofisica de Canarias.

Based on observations made with the Gran Telescopio Canarias (GTC), instaled in the Spanish Observatorio del Roque de los Muchachos of the Instituto de Astrofsica de Canarias, in the island of La Palma.

The Liverpool Telescope is operated by Liverpool John Moores University at the Observatorio del Roque de los Muchachos of the Instituto de Astrofísica de Canarias. The Faulkes Telescopes are owned by Las Cumbres Observatory. CGM acknowledges support from the Royal Society, the Wolfson Foundation and the Science and Technology Facilities Council.

Additionally, we thank the RATIR project team and the staff of the Observatorio Astronmico Nacional on Sierra San Pedro Mrtir. RATIR is a collaboration between the University of California, the Universidad Nacional Autonma de México, NASA Goddard Space Flight Center, and Arizona State University, benefiting from the loan of an H2RG detector and hardware and software support from Teledyne Scientific and Imaging. RATIR, the automation of the Harold L. Johnson Telescope of the Observatorio Astronómico Nacional on Sierra San Pedro Mártir, and the operation of both are funded through NASA grants NNX09AH71G, NNX09AT02G, NNX10AI27G, and NNX12AE66G, CONACyT grants INFR-2009-01-122785 and CB-2008-101958 , UNAM PAPIIT grant IN113810, and UC MEXUS-CONACyT grant CN 09-283.

SS acknowledges support from CONICYT through FONDECYT grant 3140534, from Basal-CATA PFB-06/2007, Iniciativa Cientifica Milenio grant P10-064-F (Millennium Center for Supernova Science), and by Project IC120009 ”Millennium Institute of Astrophysics (MAS)” of Iniciativa Científica Milenio del Ministerio de Economa, Fomento y Turismo de Chile, with input from ”Fondo de Innovación para la Competitividad, del Ministerio de Economía, Fomento y Turismo de Chile”.

Part of this work is based on observations obtained at the Gemini Observatory, which is operated by the Association of Universities for Research in Astronomy, Inc., under a cooperative agreement with the NSF on behalf of the Gemini partnership: the National Science Foundation (United States), the National Research Council (Canada), CONICYT (Chile), the Australian Research Council (Australia), Ministério da Ciência, Tecnologia e Inovação (Brazil) and Ministerio de Ciencia, Tecnología e Innovación Productiva (Argentina).

Part of the funding for GROND (both hardware as well as personnel) was generously granted from the Leibniz-Prize to Prof. G. Hasinger (DFG grant HA 1850/28-1).

References

Abazajian, K. N., Adelman-McCarthy, J. K., Agüeros, M. A., et al. 2009, ApJS, 182, 543
Alard, C., & Lupton, R. H. 1998, ApJ, 503, 325
Alard, C. 2000, A&APS, 144, 363
Arnett, W. D. 1982, ApJ, 253, 785
Arnouts, S., Cristiani, S., Moscardini, L., et al. 1999, MNRAS, 310, 540
Barthelmy, S. D., Baumgartner, W. H., Cummings, J. R., et al. 2013a, GRB Coordinates Network, 14214, 1
Barthelmy, S. D., Baumgartner, W. H., Cummings, J. R., et al. 2013b, GRB Coordinates Network, 15155, 1
Berger, E., Chornock, R., Holmes, T. R., et al. 2011, ApJ, 743, 204
Bernardini, M. G., Campana, S., Ghisellini, G., et al. 2014, MNRAS, L12
Blondin, S., & Tonry, J. L. 2007, ApJ, 666, 1024
Bloom, J. S., Kulkarni, S. R., Djorgovski, S. G., et al. 1999, Nat, 401, 453
Branch, D., Benetti, S., Kasen, D., et al. 2002, ApJ, 566, 1005
Bromberg, O., Nakar, E., Piran, T., & Sari, R. 2012, ApJ, 749, 110
Bromberg, O., Nakar, E., Piran, T., & Sari, R. 2013, ApJ, 764, 179
Bruzual, G., & Charlot, S. 2003, MNRAS, 344, 1000
Bufano, F., Pian, E., Sollerman, J., et al. 2012, ApJ, 753, 67
Butler, N., Cucchiara, A., Lee, W. H., et al. 2013a, GRB Coordinates Network, 14212, 1
Butler, N., Watson, A. M., Kutyrev, A., et al. 2013b, GRB Coordinates Network, 14237, 1
Butler, N., Watson, A. M., Kutyrev, A., et al. 2013c, GRB Coordinates Network, 15165, 1
Calzetti, D., Armus, L., Bohlin, R. C., et al. 2000, ApJ, 533, 682
Cano, Z., et al. 2011a, MNRAS, 413, 669

Cano, Z., et al. 2011b, ApJ, 740, 41C
Cano, Z. 2013, MNRAS, 434, 1098
Cano, Z., Maeda, K., & Schulze, S. 2014, MNRAS, 438, 2924
Cenko, S. B., Frail, D. A., Harrison, F. A., et al. 2011, ApJ, 732, 29
Cenko, S. B. 2013, GRB Coordinates Network, 14209, 1
Chabrier, G. 2003, PASP, 115, 763
Chester, M. M., & Hagen, L. M. Z. 2013, GRB Coordinates Network, 15168, 1
Chornock, R., et al. 2010, arXiv:1004.2262
Covino, S., Fugazza, D., D'Elia, V., & Zheng, W. 2013, GRB Coordinates Network, 14211, 1
Crowther, P. A. 2007, ARA&A, 45, 177
Cucchiara, A., & Fumagalli, M. 2013, GRB Coordinates Network, 14207, 1
Cucchiara, A., & Perley, D. 2013, GRB Coordinates Network, 15144, 1
D'Avanzo, P., Melandri, A., Steele, I., Mundell, C. G., & Palazzi, E. 2012, GRB Coordinates Network, 13551, 1
D'Elia, V., Barthelmy, S. D., Gehrels, N., et al. 2013, GRB Coordinates Network, 14204, 1
Dai, Z. G., & Lu, T. 1998, A&A, 333, L87
Dall'Osso, S., Stratta, G., Guetta, D., et al. 2011, A&A, 526, A121
De Pasquale, M., Kuin, N. P., Oates, S., et al. 2013, arXiv:1312.1648
Deng, J. S., Qiu, Y. L., Hu, J. Y., Hatano, K., & Branch, D. 2000, ApJ, 540, 452
de Ugarte Postigo, A., Castro-Tirado, A. J., Gorosabel, J., et al. 2005, A&A, 443, 841
de Ugarte Postigo, A., Thoene, C. C., Gorosabel, J., et al. 2013a, GRB Coordinates Network, 14303, 1
de Ugarte Postigo, A., Cano, Z., Thoene, C. C., et al. 2013b, Central Bureau Electronic Telegrams, 3637, 1
de Ugarte Postigo, A., Thoene, C. C., Rowlinson, A., et al. 2013c, arXiv:1308.2984
de Ugarte Postigo, A., Xu, D., Leloudas, G., et al. 2013d, Central Bureau Electronic Telegrams, 3531, 1
Drout, M. R., Soderberg, A. M., Gal-Yam, A., et al. 2011, ApJ, 741, 97
Elliott, J., Krühler, T., Greiner, J., et al. 2013, A&A, 556, A23
Fukugita, M., Shimasaku, K., & Ichikawa, T. 1995, PASP, 107, 945
Galama, T. J., et al. 1998a, Nature, 395, 670
Garnavich, P., Jha, S., Kirshner, R., et al. 1997, IAUCirc, 6786, 1
Gendre, B., Dereli, H., Atteia, J. L., Boer, M., & Klotz, A. 2013, GRB Coordinates Network, 14213, 1
Golenetskii, S., Aptekar, R., Frederiks, D., et al. 2013, GRB Coordinates Network, 15145, 1
Gorosabel, J., Jelinek, M., Wang, C., et al. 2012, GRB Coordinates Network, 13550, 1
Granot, J. 2005, ApJ, 631, 1022
Greiner, J., Bornemann, W., Clemens, C., et al. 2008, PASP, 120, 405
Grupe, D., et al. 2007, ApJ, 662, 443
Grupe, D., et al. 2010, ApJ, 711, 1008
Guidorzi, C., Clemens, C., Kobayashi, S., et al. 2009, A&A, 499, 439
Guidorzi, C., & Melandri, A. 2013, GRB Coordinates Network, 15140, 1
Hachinger, S., Mazzali, P. A., Sullivan, M., et al. 2013, MNRAS, 429, 2228
Hagen, L. M. Z., Chester, M. M., Cummings, J. R., et al. 2013, GRB Coordinates Network, 15139, 1
Harrison, R., & Kobayashi, S. 2013, ApJ, 772, 101
Hentunen, V.-P., Nissinen, M., & Salmi, T. 2013a, GRB Coordinates Network, 14216, 1
Hentunen, V.-P., Nissinen, M., Vilokki, H., & Salmi, T. 2013b, GRB Coordinates Network, 15156, 1
Hjorth, J., Sollerman, J., Møller, P., et al. 2003, Nature, 423, 847
Hjorth, J., & Bloom, J. S. 2012, Chapter 9 in "Gamma-Ray Bursts", Cambridge Astrophysics Series 51, eds. C. Kouveliotou, R. A. M. J. Wijers and S. Woosley, Cambridge University Press (Cambridge), p. 169-190, 169
Hogg, D. W., Baldry, I. K., Blanton, M. R., & Eisenstein, D. J. 2002, arXiv:astro-ph/0210394
Hook, I. M., Jørgensen, I., Allington-Smith, J. R., et al. 2004, PASP, 116, 425
Hou, S. J., Geng, J. J., Wang, K., et al. 2014, arXiv:1402.6545
Hu, J. Y., Qiu, Y. L., Qiao, Q. Y., et al. 1997, IAUCirc, 6783, 1
Im, M., & Hong, J. 2012, GRB Coordinates Network, 13544, 1
Ishida, Y., Tashiro, M., Terada, Y., et al. 2013, GRB Coordinates Network, 14245, 1
Iwamoto, K., et al. 1998, Nature, 395, 672
Izzo, L., & D'Avino, L. 2013, GRB Coordinates Network, 15153, 1
Jakobsson, P., Hjorth, J., Fynbo, J. P. U., et al. 2003, A&A, 408, 941
Jakobsson, P., Hjorth, J., Fynbo, J. P. U., et al. 2004, A&A, 427, 785
Japelj, J., Gomboc, A., Kopac, D., et al. 2014, arXiv:1402.3701
Jester, S., et al. 2005, AJ, 130, 873
Kann, D. A., Klose, S., & Zeh, A. 2006, ApJ, 641, 993
Kann, D. A., Klose, S., Zhang, B., et al. 2010, ApJ, 720, 1513
Kasen, D., Thomas, R. C., & Nugent, P. 2006, ApJ, 651, 366
Khorunzhev, G., Burenin, R., Pavlinsky, M., et al. 2013, GRB Coordinates Network, 15244, 1
Klose, S., Greiner, J., Fynbo, J., et al. 2012, GRB Coordinates Network, 13613, 1
Klose, S., Nicuesa Guelbenzu, A., Kruehler, T., et al. 2013, GRB Coordinates Network, 15320, 1
Knust, F., Varela, K., Greiner, J., & Kann, D. A. 2013, GRB Coordinates Network, 14221, 1
Kobayashi, S. 2000, ApJ, 545, 807
Krühler, T., Greiner, J., Schady, P., et al. 2011, A&A, 534, A108
Krühler, T., Fynbo, J. P. U., Geier, S., et al. 2012, A&A, 546, A8
Kumar, P., & Piran, T. 2000, ApJ, 532, 286
Kuroda, D., Yanagisawa, K., Shimizu, Y., et al. 2013, GRB Coordinates Network, 14220, 1
Landolt, A. U. 1992, AJ, 104, 340
Laskar, T., Zauderer, A., & Berger, E. 2012, GRB Coordinates Network, 13547, 1
Laskar, T., Zauderer, A., & Berger, E. 2013, GRB Coordinates Network, 15162, 1
Leonini, S., Guerrini, G., Rosi, P., & Tinjaca Ramirez, L. M. 2013, GRB Coordinates Network, 15150, 1
Levan, A. J., Tanvir, N. R., Fruchter, A. S., et al. 2013, arXiv:1307.5338
Leventis, K., Wijers, R. A. M. J., & van der Horst, A. J. 2014, MNRAS, 437, 2448
Levesque, E. M., Kewley, L. J., Graham, J. F., & Fruchter, A. S. 2010, ApJL, 712, L26
Lü, H.-J., & Zhang, B. 2014, arXiv:1401.1562
MacFadyen, A. I., & Woosley, S. E. 1999, ApJ, 524, 262
MacFadyen, A. I., Woosley, S. E., & Heger, A. 2001, ApJ, 550, 410
Maeda, K., Mazzali, P. A., & Nomoto, K. 2006, ApJ, 645, 1331
Malesani, D., Tagliaferri, G., Chincarini, G., et al. 2004, ApJL, 609, L5
Margutti, R., Guidorzi, C., Chincarini, G., et al. 2010, MNRAS, 406, 2149
Masi, G., & Nocentini, F. 2013, GRB Coordinates Network, 15152, 1
Matheson, T., et al. 2003, ApJ, 599, 394
Maund, J. R., Reilly, E., & Mattila, S. 2014, MNRAS, 438, 938
Mazzali, P. A., & Lucy, L. B. 1993, A&A, 279, 447
Mazzali, P. A., Sullivan, M., Hachinger, S., et al. 2014, MNRAS, 286
Nakamura, T., Mazzali, P. A., Nomoto, K., & Iwamoto, K. 2001, ApJ, 550, 991
Nardini, M., Elliott, J., Filgas, R., et al. 2014, A&A, 562, A29
Nicuesa Guelbenzu, A., Kruehler, T., Greiner, J., et al. 2013, Central Bureau Electronic Telegrams, 3677, 1
Oates, S. R., & Ukwatta, T. N. 2012, GRB Coordinates Network, 13539, 1
Palmer, D. M., Barthelmy, S. D., Baumgartner, W. H., et al. 2012, GRB Coordinates Network, 13536, 1
Panaitescu, A., Meszaros, P., & Rees, M. J. 1998, ApJ, 503, 314
Perley, D. A. 2013a, GRB Coordinates Network, 14222, 1
Perley, D. A. 2013b, GRB Coordinates Network, 14227, 1
Perley, D. A., & Keating, G. 2013, GRB Coordinates Network, 14210, 1
Pian, E., et al. 2006, Nature, 442, 1011
Piran, T., Bromberg, O., Nakar, E., & Sari, R. 2013, Royal Society of London Philosophical Transactions Series A, 371, 20273
Planck Collaboration, Ade, P. A. R., Aghanim, N., et al. 2013, arXiv:1303.5076
Pozanenko, A., Volnova, A., Hafizov, B., & Burhonov, O. 2013a, GRB Coordinates Network, 15190, 1
Pozanenko, A., Volnova, A., Hafizov, B., & Burhonov, O. 2013b, GRB Coordinates Network, 15237, 1
Ransom, S. M., Hessels, J. W. T., Stairs, I. H., et al. 2005, Science, 307, 892
Rau, A., Savaglio, S., Krühler, T., et al. 2010, ApJ, 720, 862
Rau, A. 2012, GRB Coordinates Network, 13560, 1
Rees, M. J., & Meszaros, P. 1998, ApJL, 496, L1
Rhoads, J. E. 1997, ApJL, 487, L1
Richardson, D. 2009, AJ, 137, 347
Rowlinson, A., O'Brien, P. T., Metzger, B. D., Tanvir, N. R., & Levan, A. J. 2013, MNRAS, 430, 1061
Sari, R., Piran, T., & Narayan, R. 1998, ApJL, 497, L17
Sari, R., & Mészáros, P. 2000, ApJL, 535, L33
Savaglio, S., Rau, A., Greiner, J., et al. 2012, MNRAS, 420, 627
Schlegel, D. J., Finkbeiner, D. P., & Davis, M. 1998, ApJ, 500, 525
Schulze, S., Leloudas, G., Xu, D., et al. 2013, Central Bureau Electronic Telegrams, 3587, 1
Schulze, S., Malesani, D., Cucchiara, A., et al. 2014, arXiv:1401.3774
Singer, L. P., Cenko, S. B., & Brown, D. A. 2013, GRB Coordinates Network, 14244, 1
Smartt, S. J., Eldridge, J. J., Crockett, R. M., & Maund, J. R. 2009, MNRAS, 395, 1409
Smith, I. A., Tilanus, R. P. J., Tanvir, N. R., & Frail, D. A. 2012, GRB Coordinates Network, 13554, 1

Smith, I. A., Tilanus, R. P. J., Tanvir, N. R., & Frail, D. A. 2013, GRB Coordinates Network, 15174, 1
Sollerman, J., et al. 2006, A& A, 454, 503
Sonbas, E., Temiz, U., Guver, T., et al. 2013, GRB Coordinates Network, 15161, 1
Sparre, M., Sollerman, J., Fynbo, J. P. U., et al. 2011, ApJL, 735, L24
Stanek, K. Z., et al. 2003, ApJL, 591, L17
Strolger, L.-G., Riess, A. G., Dahlen, T., et al. 2004, ApJ, 613, 200
Thomas, R. C., Nugent, P. E., & Meza, J. C. 2011, PASP, 123, 237
Thöne, C. C., Kann, D. A., Jóhannesson, G., et al. 2010, A&A, 523, A70
Troja, E., Cusumano, G., O'Brien, P. T., et al. 2007, ApJ, 665, 599
Trotter, A., Haislip, J., Lacluyze, A., et al. 2013, GRB Coordinates Network, 15148, 1
Virgili, F. J., Japelj, J., Mundell, C. G., & Melandri, A. 2012, GRB Coordinates Network, 13531, 1
Volnova, A., Matkin, A., Stepura, A., Molotov, I., & Pozanenko, A. 2013a, GRB Coordinates Network, 15185, 1
Volnova, A., Minikulov, N., Gulyamov, M., Molotov, I., & Pozanenko, A. 2013b, GRB Coordinates Network, 15186, 1
Volnova, A., Linkov, V., Polyakov, K., et al. 2013, GRB Coordinates Network, 15188c, 1
Volnova, A., Krugly, Y., Slyusarev, I., Molotov, I., & Pozanenko, A. 2013d, GRB Coordinates Network, 15189, 1
Ukwatta, T. N., Burrows, D. N., Chester, M. M., et al. 2012, GRB Coordinates Network, 13530, 1
Usov, V. V. 1992, Nature, 357, 472
Woosley, S. E. 1993, ApJ, 405, 273
Woosley, S. E., & Bloom, J. S. 2006, ARA&A, 44, 507
Wren, J., Wozniak, P., Davis, H., & Vestrand, W. T. 2012, GRB Coordinates Network, 13545, 1
Wren, J., Vestrand, W. T., Wozniak, P., & Davis, H. 2013, GRB Coordinates Network, 14218, 1
Xin, L. P., Han, X. H., Qiu, Y. L., et al. 2013, GRB Coordinates Network, 15146, 1
Xu, M., Huang, Y.-F., & Lu, T. 2009, Research in Astronomy and Astrophysics, 9, 1317
Xu, D., & Zhang, T. M. 2013, GRB Coordinates Network, 14215, 1
Xu, D., de Ugarte Postigo, A., Leloudas, G., et al. 2013a, ApJ, 776, 98
Xu, D., Zhang, C. M., Cao, C., & Hu, S. M. 2013b, GRB Coordinates Network, 15142, 1
Yoshii, T., Ito, K., Saito, Y., et al. 2013, GRB Coordinates Network, 15143, 1
Younes, G., & Bhat, P. N. 2013, GRB Coordinates Network, 14219, 1
Zauderer, B. A., Laskar, T., & Berger, E. 2013, GRB Coordinates Network, 15159, 1
Zhao, X.-H., & Bai, J.-M. 2013, GRB Coordinates Network, 14217, 1
Zhang, B., & Mészáros, P. 2001, ApJL, 552, L35
Zhang, B., Fan, Y. Z., Dyks, J., et al. 2006, ApJ, 642, 354
Zheng, W., Flewelling, H., 2013a, GRB Coordinates Network, 14205, 1
Zheng, W., Flewelling, H., Guver, T., & Yuan, F. 2013b, GRB Coordinates Network, 14208, 1

Table 3. List of Photometry

GRB	Filter	$t - t_0$ (d)	$m^{\dagger}$	m_{err}	System	Telescope
120729A	g	0.7683	24.00	0.11	AB	GTC
120729A	g	18.6095	24.79	0.06	AB	GTC
120729A	g	24.6329	24.88	0.08	AB	GTC
120729A	g	189.3991	24.44	0.07	AB	GTC
120729A	r	0.7629	23.56	0.08	AB	GTC
120729A	r	8.7604	24.11	0.11	AB	GTC
120729A	r	18.5914	23.93	0.09	AB	GTC
120729A	r	20.5592	23.97	0.09	AB	GTC
120729A	r	189.3824	24.05	0.07	AB	GTC
120729A	i	0.6433	22.78	0.10	AB	TNG
120729A	i	0.7575	23.24	0.06	AB	GTC
120729A	i	18.6275	23.66	0.07	AB	GTC
120729A	i	24.6534	23.63	0.07	AB	GTC
120729A	i	189.4159	23.89	0.07	AB	GTC
120729A	z	0.7738	23.27	0.27	AB	GTC
120729A	z	189.4331	23.86	0.14	AB	GTC
120729A	B	0.0053	16.60	0.09	Vega	FTN
120729A	B	0.0079	16.89	0.08	Vega	FTN
120729A	B	0.0114	17.27	0.18	Vega	FTN
120729A	B	0.0160	17.70	0.08	Vega	FTN
120729A	B	0.0226	18.02	0.10	Vega	FTN
120729A	B	0.0354	18.35	0.10	Vega	FTN
120729A	B	0.0564	19.16	0.08	Vega	FTN
120729A	B	0.0788	19.56	0.08	Vega	FTN
120729A	B	0.6564	25.14	0.67	Vega	TNG
120729A	V	0.0060	15.91	0.10	Vega	FTN
120729A	V	0.5864	24.21	0.47	Vega	TNG
120729A	R	0.0033	15.05	0.06	Vega	FTN
120729A	R	0.0037	15.06	0.06	Vega	FTN
120729A	R	0.0041	15.21	0.07	Vega	FTN
120729A	R	0.0090	16.02	0.07	Vega	FTN
120729A	R	0.0127	16.39	0.07	Vega	FTN
120729A	R	0.0181	16.81	0.08	Vega	FTN
120729A	R	0.0254	17.09	0.08	Vega	FTN
120729A	R	0.0327	17.26	0.07	Vega	FTN
120729A	R	0.0399	17.46	0.08	Vega	FTN
120729A	R	0.0464	17.66	0.12	Vega	FTN
120729A	R	0.0500	17.70	0.10	Vega	FTN
120729A	R	0.0552	18.00	0.08	Vega	FTN
120729A	R	0.0626	18.12	0.08	Vega	FTN
120729A	R	0.0698	18.24	0.09	Vega	FTN
120729A	R	0.0771	18.54	0.08	Vega	FTN
120729A	R	0.0865	18.79	0.07	Vega	FTN
120729A	R	0.5983	22.50	0.46	Vega	LT
120729A	R	0.6301	23.23	0.18	Vega	TNG
120729A	I_c	0.0068	15.63	0.06	Vega	FTN
120729A	I_c	0.0102	16.27	0.06	Vega	FTN
120729A	I_c	0.0142	16.57	0.06	Vega	FTN
120729A	I_c	0.0202	17.03	0.07	Vega	FTN
120729A	I_c	0.0282	17.20	0.06	Vega	FTN
120729A	I_c	0.0348	17.38	0.07	Vega	FTN
120729A	I_c	0.0427	17.69	0.07	Vega	FTN
120729A	I_c	0.0474	17.80	0.09	Vega	FTN
120729A	I_c	0.0515	18.02	0.08	Vega	FTN
120729A	I_c	0.0573	18.12	0.07	Vega	FTN
120729A	I_c	0.0654	18.39	0.07	Vega	FTN
120729A	I_c	0.0719	18.48	0.09	Vega	FTN
120729A	I_c	0.0799	18.67	0.08	Vega	FTN
120729A	I_c	0.6279	22.67	0.35	Vega	LT
120729A	I_c	0.7069	¿21.3	-	Vega	IAC80
130215A	g	0.9783	20.84	0.06	AB	GROND

Table 3. List of Photometry

GRB	Filter	$t - t_0$ (d)	$m^{\dagger}$	m_{err}	System	Telescope
130215A	g	2.9563	21.73	0.21	AB	GROND
130215A	g	9.7970	22.76	0.23	AB	GTC
130215A	g	372.8488	> 26.2	-	AB	GTC
130215A	r	0.0081	14.09	0.04	AB	ROTSE
130215A	r	0.0082	14.17	0.05	AB	ROTSE
130215A	r	0.0084	14.03	0.05	AB	ROTSE
130215A	r	0.0085	14.10	0.05	AB	ROTSE
130215A	r	0.0086	14.06	0.05	AB	ROTSE
130215A	r	0.0087	14.09	0.02	AB	ROTSE
130215A	r	0.0088	14.07	0.05	AB	ROTSE
130215A	r	0.0089	14.11	0.06	AB	ROTSE
130215A	r	0.0090	14.00	0.05	AB	ROTSE
130215A	r	0.0092	14.13	0.05	AB	ROTSE
130215A	r	0.0093	14.16	0.06	AB	ROTSE
130215A	r	0.0095	14.22	0.07	AB	ROTSE
130215A	r	0.0099	14.28	0.07	AB	ROTSE
130215A	r	0.0102	14.28	0.04	AB	ROTSE
130215A	r	0.0105	14.28	0.04	AB	ROTSE
130215A	r	0.0109	14.35	0.07	AB	ROTSE
130215A	r	0.0110	14.34	0.01	AB	ROTSE
130215A	r	0.0112	14.32	0.06	AB	ROTSE
130215A	r	0.0115	14.37	0.07	AB	ROTSE
130215A	r	0.0119	14.50	0.03	AB	ROTSE
130215A	r	0.0122	14.47	0.07	AB	ROTSE
130215A	r	0.0125	14.61	0.06	AB	ROTSE
130215A	r	0.0131	14.60	0.03	AB	ROTSE
130215A	r	0.0139	14.72	0.04	AB	ROTSE
130215A	r	0.0147	14.75	0.03	AB	ROTSE
130215A	r	0.0155	14.83	0.04	AB	ROTSE
130215A	r	0.0163	14.86	0.04	AB	ROTSE
130215A	r	0.0167	14.92	0.02	AB	ROTSE
130215A	r	0.0171	15.06	0.11	AB	ROTSE
130215A	r	0.0179	15.02	0.04	AB	ROTSE
130215A	r	0.0187	15.16	0.12	AB	ROTSE
130215A	r	0.0195	15.18	0.05	AB	ROTSE
130215A	r	0.0203	15.19	0.12	AB	ROTSE
130215A	r	0.0211	15.24	0.06	AB	ROTSE
130215A	r	0.0219	15.30	0.12	AB	ROTSE
130215A	r	0.0227	15.44	0.10	AB	ROTSE
130215A	r	0.0235	15.45	0.10	AB	ROTSE
130215A	r	0.0243	15.56	0.13	AB	ROTSE
130215A	r	0.0247	15.50	0.03	AB	ROTSE
130215A	r	0.0251	15.58	0.06	AB	ROTSE
130215A	r	0.0259	15.60	0.10	AB	ROTSE
130215A	r	0.0267	15.68	0.08	AB	ROTSE
130215A	r	0.0275	15.64	0.11	AB	ROTSE
130215A	r	0.0283	15.70	0.12	AB	ROTSE
130215A	r	0.0291	15.73	0.07	AB	ROTSE
130215A	r	0.0299	15.85	0.13	AB	ROTSE
130215A	r	0.0307	15.74	0.12	AB	ROTSE
130215A	r	0.0316	15.79	0.12	AB	ROTSE
130215A	r	0.0324	15.86	0.12	AB	ROTSE
130215A	r	0.0328	15.92	0.03	AB	ROTSE
130215A	r	0.0332	15.93	0.09	AB	ROTSE
130215A	r	0.0341	16.05	0.09	AB	ROTSE
130215A	r	0.0349	15.99	0.11	AB	ROTSE
130215A	r	0.0357	16.19	0.14	AB	ROTSE
130215A	r	0.0366	16.12	0.16	AB	ROTSE
130215A	r	0.0374	16.08	0.10	AB	ROTSE
130215A	r	0.0382	16.12	0.09	AB	ROTSE
130215A	r	0.0391	16.27	0.10	AB	ROTSE

Table 3. List of Photometry

GRB	Filter	$t - t_0$ (d)	$m^{\dagger}$	m_{err}	System	Telescope
130215A	r	0.0399	16.10	0.12	AB	ROTSE
130215A	r	0.0407	16.22	0.17	AB	ROTSE
130215A	r	0.0412	16.21	0.04	AB	ROTSE
130215A	r	0.0416	16.20	0.09	AB	ROTSE
130215A	r	0.0424	16.23	0.16	AB	ROTSE
130215A	r	0.0432	16.21	0.11	AB	ROTSE
130215A	r	0.0441	16.19	0.11	AB	ROTSE
130215A	r	0.0449	16.18	0.10	AB	ROTSE
130215A	r	0.0457	16.30	0.15	AB	ROTSE
130215A	r	0.0466	16.27	0.11	AB	ROTSE
130215A	r	0.0474	16.50	0.22	AB	ROTSE
130215A	r	0.0482	16.53	0.15	AB	ROTSE
130215A	r	0.0491	16.45	0.18	AB	ROTSE
130215A	r	0.0495	16.44	0.04	AB	ROTSE
130215A	r	0.0499	16.28	0.13	AB	ROTSE
130215A	r	0.0507	16.37	0.13	AB	ROTSE
130215A	r	0.0516	16.64	0.18	AB	ROTSE
130215A	r	0.0658	16.81	0.06	AB	ROTSE
130215A	r	0.0674	16.99	0.06	AB	RATIR
130215A	r	0.0710	16.84	0.14	AB	ROTSE
130215A	r	0.0754	17.15	0.04	AB	RATIR
130215A	r	0.0765	17.15	0.08	AB	RATIR
130215A	r	0.0824	17.19	0.06	AB	RATIR
130215A	r	0.0833	17.22	0.06	AB	RATIR
130215A	r	0.0893	17.33	0.08	AB	RATIR
130215A	r	0.0928	17.41	0.09	AB	RATIR
130215A	r	0.0938	17.48	0.04	AB	RATIR
130215A	r	0.0952	17.42	0.03	AB	RATIR
130215A	r	0.0963	17.31	0.07	AB	RATIR
130215A	r	0.0973	17.43	0.06	AB	RATIR
130215A	r	0.1021	17.49	0.04	AB	RATIR
130215A	r	0.1056	17.52	0.03	AB	RATIR
130215A	r	0.1066	17.51	0.04	AB	RATIR
130215A	r	0.1102	17.68	0.05	AB	RATIR
130215A	r	0.1111	17.84	0.06	AB	RATIR
130215A	r	0.1129	17.58	0.02	AB	RATIR
130215A	r	0.1146	17.55	0.04	AB	RATIR
130215A	r	0.1202	17.85	0.09	AB	RATIR
130215A	r	0.1362	17.70	0.22	AB	ROTSE
130215A	r	0.1426	17.57	0.19	AB	ROTSE
130215A	r	0.1506	17.71	0.20	AB	ROTSE
130215A	r	0.1588	17.72	0.20	AB	ROTSE
130215A	r	0.1667	17.55	0.23	AB	ROTSE
130215A	r	0.9783	20.42	0.04	AB	GROND
130215A	r	2.0713	21.08	0.13	AB	RATIR
130215A	r	2.9563	21.19	0.09	AB	GROND
130215A	r	3.1015	21.21	0.07	AB	RATIR
130215A	r	4.0876	21.51	0.10	AB	RATIR
130215A	r	5.7866	21.54	0.09	AB	NOT
130215A	r	8.0828	22.59	0.18	AB	RATIR
130215A	r	9.7887	22.40	0.10	AB	GTC
130215A	r	13.8012	23.38	0.07	AB	NOT
130215A	r	17.5687	23.81	0.42	AB	RATIR
130215A	r	372.8629	> 26.1	-	AB	GTC
130215A	i	0.0674	16.67	0.06	AB	RATIR
130215A	i	0.0685	16.61	0.17	AB	RATIR
130215A	i	0.0730	16.79	0.10	AB	RATIR
130215A	i	0.0754	16.89	0.04	AB	RATIR
130215A	i	0.0765	16.83	0.08	AB	RATIR
130215A	i	0.0824	17.00	0.07	AB	RATIR
130215A	i	0.0833	17.06	0.07	AB	RATIR

Table 3. List of Photometry

GRB	Filter	$t - t_0$ (d)	$m^{\dagger}$	m_{err}	System	Telescope
130215A	i	0.0883	17.06	0.07	AB	RATIR
130215A	i	0.0893	17.04	0.08	AB	RATIR
130215A	i	0.0928	17.08	0.07	AB	RATIR
130215A	i	0.0938	17.22	0.03	AB	RATIR
130215A	i	0.0952	17.17	0.03	AB	RATIR
130215A	i	0.0963	17.16	0.06	AB	RATIR
130215A	i	0.0973	17.25	0.07	AB	RATIR
130215A	i	0.1021	17.26	0.04	AB	RATIR
130215A	i	0.1056	17.26	0.03	AB	RATIR
130215A	i	0.1066	17.25	0.04	AB	RATIR
130215A	i	0.1102	17.34	0.05	AB	RATIR
130215A	i	0.1111	17.29	0.05	AB	RATIR
130215A	i	0.1129	17.31	0.02	AB	RATIR
130215A	i	0.1146	17.38	0.05	AB	RATIR
130215A	i	0.1202	17.51	0.09	AB	RATIR
130215A	i	0.8175	20.04	0.05	AB	NOT
130215A	i	0.9783	20.14	0.06	AB	GROND
130215A	i	2.0713	20.98	0.14	AB	RATIR
130215A	i	2.9563	20.82	0.12	AB	GROND
130215A	i	3.1039	20.88	0.07	AB	RATIR
130215A	i	4.0543	20.88	0.08	AB	RATIR
130215A	i	4.0876	20.81	0.06	AB	RATIR
130215A	i	4.1206	20.68	0.07	AB	RATIR
130215A	i	4.7809	20.86	0.05	AB	NOT
130215A	i	5.7932	21.07	0.11	AB	NOT
130215A	i	8.0821	22.25	0.16	AB	RATIR
130215A	i	9.7910	22.39	0.12	AB	GTC
130215A	i	11.0831	22.68	0.26	AB	RATIR
130215A	i	13.7889	22.78	0.08	AB	NOT
130215A	i	17.5687	23.52	0.40	AB	RATIR
130215A	i	24.2781	23.63	0.30	AB	NOT
130215A	i	372.8358	> 25.1	-	AB	GTC
130215A	z	0.0671	16.35	0.20	AB	RATIR
130215A	z	0.0785	16.58	0.08	AB	RATIR
130215A	z	0.0842	16.64	0.07	AB	RATIR
130215A	z	0.0890	16.71	0.07	AB	RATIR
130215A	z	0.0904	17.09	0.13	AB	RATIR
130215A	z	0.0938	17.07	0.10	AB	RATIR
130215A	z	0.0959	16.98	0.04	AB	RATIR
130215A	z	0.0972	17.01	0.06	AB	RATIR
130215A	z	0.0980	17.15	0.10	AB	RATIR
130215A	z	0.1029	17.02	0.05	AB	RATIR
130215A	z	0.1077	17.07	0.06	AB	RATIR
130215A	z	0.1119	17.10	0.07	AB	RATIR
130215A	z	0.1139	17.11	0.04	AB	RATIR
130215A	z	0.1212	17.18	0.11	AB	RATIR
130215A	z	0.8296	20.03	0.04	AB	NOT
130215A	z	0.9783	19.92	0.07	AB	GROND
130215A	z	2.0719	20.46	0.27	AB	RATIR
130215A	z	2.9563	20.74	0.12	AB	GROND
130215A	z	3.1050	20.59	0.09	AB	RATIR
130215A	z	4.0855	20.63	0.09	AB	RATIR
130215A	z	5.8026	20.72	0.09	AB	NOT
130215A	z	8.0838	21.62	0.22	AB	RATIR
130215A	z	9.7940	22.27	0.14	AB	GTC
130215A	Y	2.0719	20.30	0.25	AB	RATIR
130215A	Y	3.1050	20.18	0.09	AB	RATIR
130215A	Y	4.0855	20.33	0.12	AB	RATIR
130215A	Y	8.0838	21.14	0.27	AB	RATIR
130215A	J	0.0754	16.38	0.10	AB	RATIR
130215A	J	0.0842	16.29	0.10	AB	RATIR

Table 3. List of Photometry

GRB	Filter	$t - t_0$ (d)	$m^{\dagger}$	m_{err}	System	Telescope
130215A	J	0.0890	16.41	0.09	AB	RATIR
130215A	J	0.0904	16.71	0.15	AB	RATIR
130215A	J	0.0939	16.31	0.10	AB	RATIR
130215A	J	0.0941	16.65	0.04	AB	RATIR
130215A	J	0.0959	16.56	0.04	AB	RATIR
130215A	J	0.0980	16.64	0.10	AB	RATIR
130215A	J	0.1028	16.66	0.06	AB	RATIR
130215A	J	0.1077	16.97	0.08	AB	RATIR
130215A	J	0.1119	16.71	0.08	AB	RATIR
130215A	J	0.1139	16.79	0.07	AB	RATIR
130215A	J	0.1212	16.82	0.12	AB	RATIR
130215A	J	0.9786	19.39	0.15	AB	GROND
130215A	J	2.0720	20.47	0.41	AB	RATIR
130215A	J	2.9611	20.08	0.26	AB	GROND
130215A	J	3.1050	20.06	0.09	AB	RATIR
130215A	J	4.0883	20.14	0.14	AB	RATIR
130215A	J	8.0842	21.55	0.50	AB	RATIR
130215A	J	331.8415	> 23.2	-	Vega	CAHA
130215A	H	0.0941	15.48	0.17	AB	RATIR
130215A	H	0.9786	18.97	0.13	AB	GROND
130215A	H	2.0720	19.54	0.19	AB	RATIR
130215A	H	2.9611	19.94	0.31	AB	GROND
130215A	H	3.1050	19.79	0.10	AB	RATIR
130215A	H	4.0883	19.78	0.13	AB	RATIR
130215A	K	0.9786	18.63	0.22	AB	GROND
130215A	K	2.9611	18.93	0.23	AB	GROND
130831A	B	2.0525	22.700	0.070	Vega	MAO
130831A	R_c	2.0411	22.200	0.090	Vega	MAO
130831A	R_c	3.3168	22.200	0.110	Vega	Mondy
130831A	R_c	4.1061	22.530	0.090	Vega	Mondy
130831A	R_c	4.2555	22.530	0.070	Vega	MAO
130831A	R_c	5.2440	22.880	0.130	Vega	CrAO
130831A	R_c	5.2658	22.870	0.060	Vega	MAO
130831A	R_c	7.0446	22.990	0.080	Vega	MAO
130831A	R_c	8.0586	22.900	0.060	Vega	MAO
130831A	R_c	9.2558	23.110	0.060	Vega	MAO
130831A	R_c	10.2526	22.940	0.080	Vega	MAO
130831A	R_c	11.2419	22.930	0.110	Vega	MAO
130831A	R_c	15.2202	22.870	0.080	Vega	MAO
130831A	R_c	16.2715	22.770	0.070	Vega	MAO
130831A	R_c	22.0721	22.530	0.290	Vega	MAO
130831A	R_c	27.0558	22.900	0.170	Vega	MAO
130831A	R_c	28.6928	22.910	0.094	Vega	WHT
130831A	R_c	30.15945	23.360	0.160	Vega	MAO
130831A	R_c	37.1378	23.590	0.160	Vega	MAO
130831A	R_c	40.60034	23.640	0.230	Vega	Mondy
130831A	R_c	44.5578	> 23.2	-	Vega	Mondy
130831A	R_c	66.3495	23.650	0.150	Vega	CrAO
130831A	R_c	96.0754	23.750	0.350	Vega	Mondy
130831A	I_c	28.6701	22.076	0.129	Vega	WHT
130831A	g	0.3834	19.672	0.022	AB	NOT
130831A	g	4.6225	23.464	0.034	AB	WHT
130831A	r	0.3907	19.324	0.026	AB	NOT
130831A	r	0.6974	20.423	0.025	AB	NOT
130831A	r	0.7013	20.432	0.027	AB	NOT
130831A	r	7.5947	22.995	0.048	AB	NOT
130831A	r	13.4525	23.038	0.094	AB	NOT
130831A	r	68.5157	23.922	0.051	AB	Gemini
130831A	r	156.3151	24.063	0.089	AB	NOT
130831A	i	0.3901	19.100	0.027	AB	NOT
130831A	i	1.6584	21.741	0.066	AB	NOT

Table 3. List of Photometry

GRB	Filter	$t - t_0$ (d)	$m^{\dagger}$	m_{err}	System	Telescope
130831A	i	3.6759	22.403	0.053	AB	NOT
130831A	i	4.6024	22.540	0.044	AB	WHT
130831A	i	13.4761	22.580	0.061	AB	NOT
130831A	i	22.6051	22.422	0.058	AB	NOT
130831A	i	68.5281	23.777	0.089	AB	Gemini
130831A	i	127.2841	24.235	0.097	AB	LT
130831A	z	0.3987	19.026	0.043	AB	NOT
130831A	z	1.4975	21.218	0.099	AB	LT
130831A	z	6.5690	22.720	0.112	AB	LT
130831A	z	17.5640	22.726	0.200	AB	LT

Table 3. † Apparent magnitudes of the AG+SN+host are not corrected for foreground or rest-frame extinction.

[1] Centre for Astrophysics and Cosmology, Science Institute, University of Iceland, Reykjavik, Iceland.
[2] Instituto de Astrofísica de Andalucía (IAA-CSIC), Glorieta de la Astronomía s/n, E-18008, Granada, Spain.
[3] Dark Cosmology Centre, Niels Bohr Institute, Juliane Maries Vej 30, Copenhagen Ø, D-2100, Denmark.
[4] Space Research Institute, 117997, 84/32 Profsoyuznaya str., Moscow, Russia.
[5] School of Earth and Space Exploration, Arizona State University, Tempe, AZ 85287, USA.
[6] Department of Physics, University of Ferrara, via Saragat 1, I-44122 Ferrara, Italy.
[7] European Southern Observatory, Alonso de Córdova 3107, Vitacura, Casilla 19001, Santiago 19, Chile.
[8] Instituto de Astrofísica de Andalucía (IAA-CSIC), Glorieta de la Astronomía s/n, E-18008, Granada, Spain.
[9] Unidad Asociada Grupo Ciencia Planetarias UPV/EHU-IAA/CSIC, Departamento de Física Aplicada I, E.T.S. Ingeniería, Universidad del País-Vasco UPV/EHU, Alameda de Urquijo s/n, E-48013 Bilbao, Spain.
[10] Ikerbasque, Basque Foundation for Science, Alameda de Urquijo 36-5, E-48008 Bilbao, Spain.
[11] Astrophysics Research Institute, Liverpool John Moores University, Liverpool Science Park, 146 Brownlow Hill, Liverpool L3 5RF.
[12] INAF/Brera Astronomical Observatory, via Bianchi 46, 23807, Merate (LC), Italy.
[13] Department of Physics and Astronomy, University of Leicester, Leicester LE1 7RH, UK.
[14] Instituto de Astrofísica, Facultad de Física, Pontificia Universidad Católica de Chile, Av. Vicuña Mackenna 4860, Santiago, Chile.
[15] Millennium Center for Supernova Science.
[16] Faculty of Mathematics & Physics, University of Ljubljana, Jadranska ulica 19, 1000 Ljubljana, Slovenia.
[17] Centre of Excellence SPACE-SI, Aškerčeva cesta 12, 1000 Ljubljana, Slovenia.
[18] The Oskar Klein Centre, AlbaNova, SE-106 91 Stockholm, Sweden.
[19] Department of Astronomy, University of California, Berkeley, CA 94720-3411, USA.
[20] Max-Planck-Institut für extraterrestrische Physik, Giessenbachstraße, D-85748 Garching, Germany.
[21] Thüringer Landessternwarte Tautenburg, Sternwarte 5, D-07778 Tautenburg, Germany.
[22] Department of Physics, University of Michigan, Ann Arbor, MI 48109, USA.
[23] Department of Physics, Southern Methodist University, Dallas, Texas 75275, USA
[24] Institute for Astronomy, University of Hawaii, 2680 Woodlawn Drive, Honolulu HI 96822, USA.
[25] Department of Astronomy and Space Sciences, Istanbul University Science Faculty, 34119 Istanbul, Turkey.
[26] Astronomical Institute, University of Amsterdam, Science Park 904, NL-1098 XH Amsterdam, the Netherlands.
[27] Department of Physics, University of Warwick, Coventry CV4 7AL, UK.
[28] Research School of Astronomy and Astrophysics, The Australian National University, Weston Creek, ACT 2611, Australia.
[29] Isaac Newton Group of Telescopes, Apartado de Correos 321, E-38700 Santa Cruz de La Palma, Canary Islands, Spain.
[30] Centre for Astronomy and Particle Theory, University of Nottingham, UK.
[31] Ulugh Beg Astronomical Institute, 100052, 33 Astronomicheskaya str., Tashkent, Uzbekistan.
[32] Institute of Solar-Terrestrial Physics, Siberian department of the Russian Academy of Sciences, 664033, p/o box 291; Lermontov str., 126a, Irkutsk, Russia.
[33] Institute of Astronomy of Kharkiv National University, 61022, 35 Sumska str., Kharkiv, Ukraine.
[34] JSC Asronomical Scientific Center, Svobody str., 35, 22, 125362, Moscow, Russia.
[35] Ussuriysk Astrophysical Observatory, 692533, Primorskiy kray, Ussuriyskiy rayon, s. Gornotayozhnoe, Russia.
[36] Institute of Astrophysics, Academy of Sciences of Tajikistan, 734042, Bukhoro Str. 22, Dushanbe, Tajikistan.
[37] Keldysh Institute of Applied Mathematics, 125047, 4, Miusskaya sq., Moscow, Russia.
[38] Crimean Astrophysical Observatory, Taras Shevchenko National University of Kyiv, 98409, pgt. Nauchny, Crimea, Ukraine.
[39] School of Physics and Astronomy, University of Nottingham, UK.
[40] STFC Rutherford Fellow.